Experimental studies on mixing of yield stress fluids in a magnetic stirrer

Mohammad Omidi

A Thesis

in

The Department

of

Mechanical and Industrial Engineering

Presented in Partial Fulfillment of the Requirements

for the Degree of

Master of Applied Science (Mechanical Engineering) at

Concordia University

Montréal, Québec, Canada

December 2023

CONCORDIA UNIVERSITY

School of Graduate Studies

This is to certify that the thesis prepared

By: **Mohammad Omidi**

Entitled: **Experimental studies on mixing of yield stress fluids in a magnetic stirrer**

and submitted in partial fulfillment of the requirements for the degree of

Master of Applied Science (Mechanical Engineering)

complies with the regulations of this University and meets the accepted standards with respect to originality and quality.

Signed by the Final Examining Committee:

_____ Chair
Dr. Martin D. Pugh

_____ External Examiner
Dr. Alex De Visscher

_____ Examiner
Dr. Marius Paraschivoiu

_____ Supervisor
Dr. Ida Karimfazli

Approved by _____
Martin D. Pugh, Chair
Department of Mechanical and Industrial Engineering

_____ 2023

_____
Mourad Debbabi, Dean
Faculty of Engineering and Computer Science

Abstract

Experimental studies on mixing of yield stress fluids in a magnetic stirrer

Mohammad Omidi

Yield stress fluids exhibit a distinctive flow behavior characterized by a persistent resistance to flow until an external force surpasses their yield stress threshold. In this thesis, we investigate mixing characteristics of yield stress fluids within a magnetic mixer. The experimental apparatus comprises an acrylic rectangular mixing vessel and a high-capacity magnetic stirrer. Rheological properties of Carbopol gels were meticulously analyzed, and the yield stress was precisely determined by fitting the data with the Herschel Bulkley model. The study utilizes both Particle Image Velocimetry (PIV) and Dye Visualization techniques to comprehensively characterize the flow dynamics. Stirring characteristics, including velocity norm and cavern formation, were systematically investigated in both transient and periodic states. Notably, our experimental findings unveil a distinct trend: as the ratio of inertial forces to viscous forces increases, there is a noticeable shift in the growth rate of velocity norm and cavern area, indicative of the increasing dominance of inertial forces. Moreover, our research employing the Dye Visualization method demonstrates that the cavern's shape remains consistent regardless of the position of the rod. In contrast, PIV results reveal that at lower ratios of inertial to viscous forces, the rod's position significantly influences the cavern's shape.

Acknowledgments

I would like to express my deepest gratitude to my supervisor, Dr. Ida Karimfazli, for her invaluable guidance, continuous support, and unwavering encouragement throughout the journey of completing this thesis. Her expertise, insightful feedback, and dedication have been instrumental in shaping the direction and quality of this work. I am truly grateful for her mentorship and the opportunities provided to me during this research endeavor.

I am immensely grateful to Dr. Wael for his invaluable assistance in teaching me the fundamentals of PIV system hardware. I extend my deepest thanks for the dedicated time he devoted to guiding me in this area of study.

I would like to express my heartfelt gratitude to my parents and all my loved ones, as well as my friends and colleagues, for their unwavering support throughout my graduate program. Their constant presence and encouragement have meant the world to me, and I am truly thankful for their steadfast support.

Contents

List of Figures

List of Tables

Chapter 1

Introduction

1.1 Importance of mixing

Mixing is the process of eliminating non-uniformity in a substance. To manufacture and produce new materials in different industries, it is necessary to mix two or more fluids. This makes mixing one of the most common processes in engineering applications. The application of mixing is not confined to combining different materials or reducing the concentration gradient. It can be used for various purposes, such as increasing heat and mass transfer and improving aeration efficiency. For example, mixing is used in the food industry to increase the temperature uniformly and change the food structure (Paul, Atiemo-Obeng, & Kresta, 2004).

Mixing determines the homogeneity of the final product. In 1990, it was evaluated that the lack of knowledge of mixing process costs $10 billion per year in the United States of America (Bowler, Bakalis, & Watson, 2020). Mixing of non-Newtonian fluids, such as yield stress fluids, is extremely complex. Yield stress fluids have various applications in different industries due to their unique flow behavior. Yield stress fluids are used in the production of food products such as sauces, dressings, and spreads. Also, they are utilized in the formulation of creams, lotions, and gels. Here, we present a brief summary of the literature and identify some research gaps in the understanding of the hydrodynamics of mixing of yield stress fluids.

1.2 Yield stress fluids

Yield stress fluids are used in many industries (Aref et al., 2017; Paul et al., 2004; Saramito & Wachs, 2017). They are often modeled using viscoplastic models. Some common examples of viscoplastic fluids are clay, gels, emulsions, bread dough, slurries, and toothpaste. Viscoplastic fluids are unyielded when the shear stress is less than a certain value called the yield stress. When unyielded, they behave like solids. On the other hand, when the applied shear stress is more than the yield stress, the material flows like a fluid. This behavior significantly affects the mixer performance, mixing quality, and power consumption when viscoplastic fluids are agitated. In fact, the existence of yielded and unyielded regions in the mixer makes the prediction of the flow behavior of this kind of material extremely hard.

Carbopol and xanthan gum are the most commonly used yield stress fluids for experimental research. Carbopol solution is a transparent gel and it is usually prepared by adding Carbopol powder with specific concentrations to the distilled water. However, the aqueous xanthan gum solution is opaque.

1.2.1 Viscoplastic models

The apparent viscosity is defined according to equation (1).

$$\hat{\eta}(\hat{\dot{\gamma}}) = \frac{\hat{\tau}}{\hat{\dot{\gamma}}} \tag{1}$$

Here $\hat{\eta}$, $\hat{\tau}$, and $\hat{\dot{\gamma}}$ are apparent viscosity, the second invariant of stress tensor, and the second invariant of strain rate tensor called shear rate, respectively,

$$\hat{\tau} = \sqrt{\frac{1}{2}\sum_{i,j=1}^{3} \hat{\tau}_{ij}^2} \tag{2}$$

$$\hat{\dot{\gamma}} = \sqrt{\frac{1}{2}\sum_{i,j=1}^{3} \hat{\dot{\gamma}}_{ij}^2} \tag{3}$$

where $\hat{\tau}_{ij}$ is the deviatoric stress tensor and $\hat{\dot{\gamma}}_{ij}$ is the strain rate tensor given by:

$$\hat{\dot{\gamma}}_{ij} = \frac{\partial \hat{u}_j}{\partial \hat{x}_i} + \frac{\partial \hat{u}_i}{\partial \hat{x}_j} \tag{4}$$

where $\hat{u}_i$ and $\hat{x}_i$ are the velocity and coordinate in the i_{th} direction. Viscoplastic fluids are commonly modeled using the Bingham or Herschel-Bulkley models (Irgens, 2014). The Bingham model defines the apparent viscosity using equation (5).

$$\hat{\eta}(\hat{\dot{\gamma}}) = \frac{\hat{\tau_y}}{\hat{\dot{\gamma}}} + \hat{\mu}_p \quad \text{iff} \quad \hat{\tau} > \hat{\tau_y} \tag{5}$$

where $\hat{\mu}_p$ is the plastic viscosity. Hence, the tensorial form of the shear stress in Bingham fluid is:

$$\begin{cases} \hat{\dot{\gamma}} = 0 \quad \text{iff} \quad \hat{\tau} < \hat{\tau_y} \\ \hat{\tau}_{ij} = \hat{\tau}_y \dfrac{\hat{\dot{\gamma}}_{ij}}{\hat{\dot{\gamma}}} + \hat{\mu}_p \hat{\dot{\gamma}}_{ij} \quad \text{iff} \quad \hat{\tau} > \hat{\tau_y} \end{cases} \tag{6}$$

Also, the simplified Bingham model for a unidirectional flow is as follows.

$$\hat{\tau} = \hat{\tau}_y + \hat{\mu}_p \hat{\dot{\gamma}} \tag{7}$$

Another common model is the Herschel-Bulkley model. Equation (8) presents the definition of apparent viscosity based on this model.

$$\hat{\eta}(\hat{\dot{\gamma}}) = \frac{\hat{\tau}_y}{\hat{\dot{\gamma}}} + \hat{K}\hat{\dot{\gamma}}^{n-1} \quad \text{iff} \quad \hat{\tau} > \hat{\tau_y} \tag{8}$$

where $\hat{K}$ is the consistency and n is the power-law index. When the value of n is less than one, the apparent viscosity decreases with the shear rate. A unidirectional Herschel-Bulkley fluid can be modeled by equation (9).

$$\begin{cases} \hat{\dot{\gamma}} = 0 \quad \text{iff} \quad \hat{\tau} < \hat{\tau_y} \\ \hat{\tau} = \hat{\tau}_y + \hat{K}\hat{\dot{\gamma}}^n \quad \text{iff} \quad \hat{\tau} > \hat{\tau_y} \end{cases} \tag{9}$$

In most studies, the rheological properties of Carbopol and xanthan gum solutions are modeled

by the Herschel-Bulkley model (Ameur, 2016a; Ameur et al., 2015; Ein-Mozaffari & Upreti, 2009; A. W. Russell et al., 2019).

1.3 Mixing characteristics

In this section, we discuss how the mixing of yield stress fluids is characterized. Three main parameters are often used to assess the mixing process: cavern dimensions, power consumption, and mixing time (see e.g., Ein-Mozaffari and Upreti (2009); A. W. Russell et al. (2019)). The cavern is commonly defined as the subdomain where the fluid velocity is not negligible (i.e. the fluid is flowing) (Arratia, Kukura, Lacombe, & Muzzio, 2006). A. W. Russell et al. (2019) visualized cavern dimensions by injecting food dye near the impeller tip (more details in section 1.5.1). They defined the boundary of the cavern as the sharp transition from a colored to a non-colored area when the cavern size and shape have reached the steady-state. They also introduced another criterion based on which the cavern is a region where the velocity exceeds 0.01 m/s. Hirata, Nienow, and Moore (1994) defined the cavern as the region where the velocity magnitude exceeds 1 % of the impeller tip velocity. The region where fluid flow is negligible is often referred to as the dead zone (rigid zone) (Ameur, 2016a; Savreux et al., 2007). It is often assumed that the fluid is well-mixed within the cavern and, therefore, a larger cavern indicates improved mixing.

Another parameter that is used to characterize the mixing process is the power consumption. The power consumption is the power that is supplied by a motor to rotate the impeller. In addition, some studies evaluate mixing by measuring the mixing time. In this method, a tracer is injected into the vessel and mixing is characterized by measuring the spatiotemporal development of the concentration of the tracer. Mixing time is typically defined as the time needed for the tracer concentration to reach 95% of its steady-state value. (Ein-Mozaffari & Upreti, 2009; Kazemzadeh et al., 2016; Pakzad et al., 2008a; Prajapati & Ein-Mozaffari, 2009).

1.4 Experimental methods

Various experimental techniques have been developed to study mixing in a stirred tank. Commonly used techniques are dye visualization Amanullah et al. (1997); Amanullah, Hjorth, and

Nienow (1998); Amanullah, Serrano-Carreon, Castro, Galindo, and Nienow (1998); Galindo et al. (1996); Galindo and Nienow (1993); Galindot and Nienow (1992); A. W. Russell et al. (2019), tracer techniques Elson, Cheesman, and Nienow (1986); Jaworski, Pacek, and Nienow (1994), dynamic conductivity tests Patel, Ein-Mozaffari, and Mehrvar (2012); Saeed and Ein-Mozaffari (2008); Saeed, Ein-Mozaffari, and Upreti (2008), hot-film anemometry (HFA) Solomon, Elson, Nienow, and Pace (1981), laser Doppler anemometry (LDA) Hirata et al. (1994), ultrasound Doppler velocimetry (UDV) Ein-Mozaffari and Upreti (2009); Hui, Bennington, and Dumont (2009); Ihejirika and Ein-Mozaffari (2007); Pakzad, Ein-Mozaffari, and Chan (2008b); Saeed, Ein-Mozaffari, and Upreti (2007), planar laser-induced fluorescence (PLIF) Adams and Barigou (2007); Arratia et al. (2006), particle image velocimetry (PIV) Cortada-Garcia et al. (2017, 2018); Sossa-Echeverria and Taghipour (2014, 2015), and electrical resistance tomography (ERT) Pakzad et al. (2008a); Pakzad, Ein-Mozaffari, and Chan (2008c); Pakzad, Ein-Mozaffari, Upreti, and Lohi (2013b, 2013c). Below, a few of these methods are briefly introduced.

• **Dye visualization**

Dye visualization has been used to observe the development of caverns in viscoplastic fluids. In this method, a small volume of ink is injected close to the impeller before the experiment starts. When stirring starts, the ink is spread in the vessel. The spreading of the ink leads to the formation of a colored region around the impeller. The colored region often grows with time before approaching a steady shape. The steady shape of the colored region is often identified as the cavern. For example, Galindo and Nienow (Galindo et al., 1996; Galindo & Nienow, 1993; Galindot & Nienow, 1992) used this visualization technique to measure cavern dimensions. The mechanically stirred vessel is shown in Fig. 1.1a. They injected methylene blue solutions near the blade tip. Amanullah et al. (Amanullah et al., 1997; Amanullah, Hjorth, & Nienow, 1998; Amanullah, Serrano-Carreon, et al., 1998) injected a solution of Crystal violet dye near the impeller hub to observe the cavern formation in a stirred tank filled with Carbopol solution. The flow setup used by them is shown in Fig. 1.1b. By injecting a solution of blue food dye and taking images when the cavern is steady, A. W. Russell et al. (2019) measured the height of caverns at different Carbopol concentrations. More details on their findings are provided in section 1.5.1.

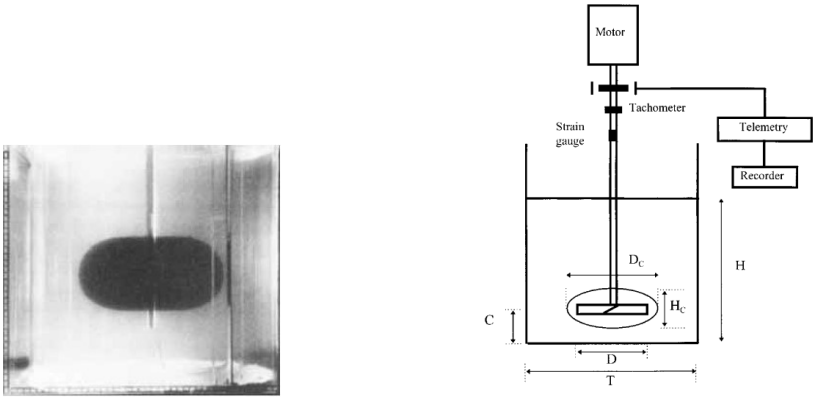

(a) (b)

Figure 1.1: (a) Photograph of well-mixed cavern created by a Scaba impeller in a Carbopol solution (Galindo et al., 1996); (b) Schematic of the configuration used by Amanullah et al. (1997).

• **Tracer technique**

Passive tracer particles are used to observe the fluid motion and cavern size in the mixing zone. Elson et al. (1986) studied the mixing of an opaque viscoplastic fluid and visualized the flow field and cavern dimensions by using the X-ray heavy metal tracer method. They added Lead (Pb) or Barium (Ba) as the heavy metal tracer to the solution and X-ray cine film was used to see the motion of tracers. Jaworski et al. (1994) used a new tracer technique by adding spherical alumina particles to the fluid. They tracked the particles by using a laser light sheet and stereo-microscope camera.

• **PIV**

PIV is a nonintrusive flow measurement technique which can be used to characterize the velocity field in a 2D cross-section or 3D subdomain of the flow. In this method, small and neutrally buoyant seeding particles are introduced to the fluid to reveal the fluid motion. To take a photo by using a camera, particles should be illuminated by the laser. To measure the velocity of particles, two successive images are captured. Each image is divided into small areas named interrogation windows which include a number of seeding particles (Raffel et al., 2018). By characterizing the displacement of particles and time interval between two images, each interrogation window produces a velocity vector. PIV method has been used by Cortada-Garcia et al. (2017, 2018) to characterize the flow field in mixing yield stress fluids. Sossa-Echeverria and Taghipour (2014, 2015) studied the

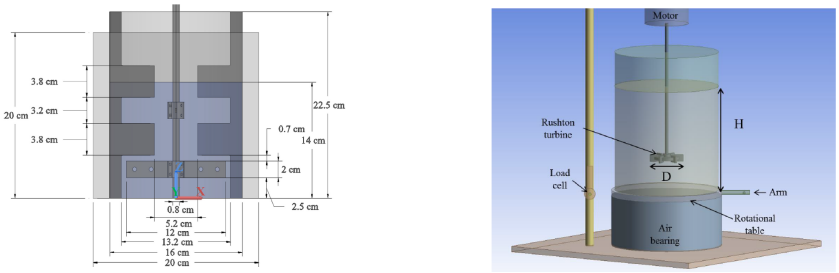

(a) (b)

Figure 1.2: (a) The side view of the flow setup used by Cortada-Garcia et al. (2018); (b) Schematic of the configuration used by Cortada-Garcia et al. (2017).

velocity field around the impeller blades in a stirred tank by using PIV.

1.5 Literature review

Studies on the hydrodynamics of mixing can be divided into two categories. The main goal of the first group of studies is to investigate the effect of fluid rheology, such as yield stress, and operating conditions, such as impeller speed, on the mixing process. On the other hand, the other group characterizes the mixing performance by considering the effect of geometrical parameters, such as impeller and vessel dimensions. It should be noted that test fluids used in all studies covered here are homogeneous (a fluid with uniform properties).

1.5.1 The effect of fluid rheology and operating conditions

Cortada-Garcia et al. (2018) used a complex lab-scale mixer that is employed for mixing of high viscosity material in different industrial applications (Figure 1.2a). They created holes on impeller blades and characterized the flow field generated by this type of impeller both experimentally and numerically. They used PIV to measure the average velocity field. One of the main conclusions is that by increasing the viscosity and shear thinning of the fluid, the characteristic velocity decreased. They also found that the existence of holes on the blades can increase the local shear rate and postulated that this could improve mixing. In another work (Cortada-Garcia et al., 2017), they developed a CFD model for a tank equipped with Rushton turbine (RT) impellers (Figure 1.2b). They showed that by increasing the shear thinning, the torque exerted by the impeller increased. A. W. Russell et

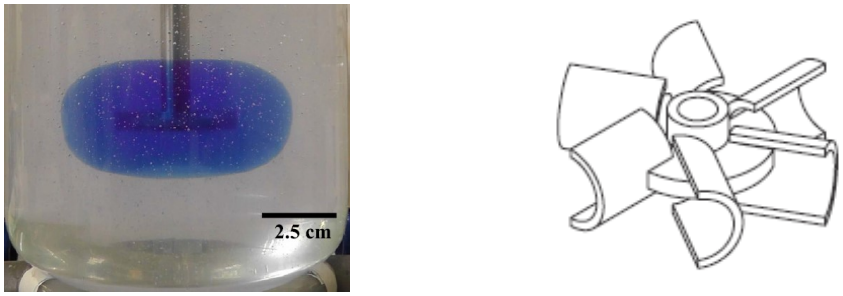

(a) (b)

Figure 1.3: (a) The side view of the mixing tank used by A. W. Russell et al. (2019); (b) Scaba 6SRGT impeller used by Pakzad et al. (2008a).

al. (2019) investigated the effect of impeller speed and fluid rheology on the cavern size and shape. They used dye visualization technique and CFD to study the mixing of Carbopol solutions by using RT impellers (Figure 1.3a). To produce a given cavern size, higher rotational speed was needed when the rheological features, such as yield stress and consistency, increased. Sossa-Echeverria and Taghipour (2015) applied a CFD model to investigate the mixing of Carbopol solutions with different concentrations by using a cylindrical tank equipped with axial flow impellers. They found rheological properties have a considerable effect on the velocity components around the impeller. At lower viscosities, the axial flow direction is dominant. Pakzad et al. (2008a) used both experimental and numerical approaches to investigate the mixing time when xanthan gum solution is agitated in a cylindrical vessel supplied with a Scaba 6SRGT impeller (Figure 1.3b). The effect of impeller speed and rheological properties on the mixing time was considered. Based on their results, the time required for tracers to be uniformly distributed increased when the value of yield stress increased.

Kazemzadeh et al. (2016) studied the effect of rheological parameters of xanthan gum solutions on power consumption and mixing time both experimentally and numerically. They used a coaxial mixing system shown in Fig. 1.4. Their studies showed that at higher values of yield stress and consistency, both power consumption and mixing time increased. However, by increasing the power-law index, the mixing time and power consumption decreased. Savreux et al. (2007) employed numerical methods to study the mixing of viscoplastic fluids in a rotating stirring tank equipped with a stationary anchor impeller (Figure 1.5a). They observed that vortices (formed when a Newtonian fluid was used) were eliminated when a fluid with low yield stress was used. In addition,

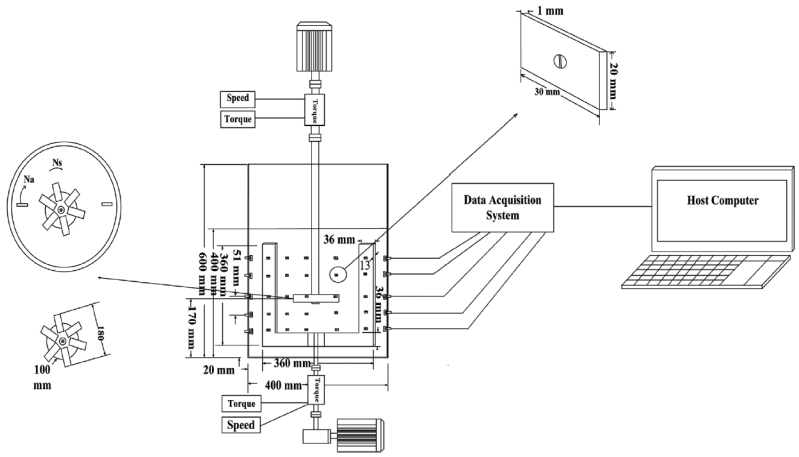

Figure 1.4: Schematic of the configuration used by Kazemzadeh et al. (2016).

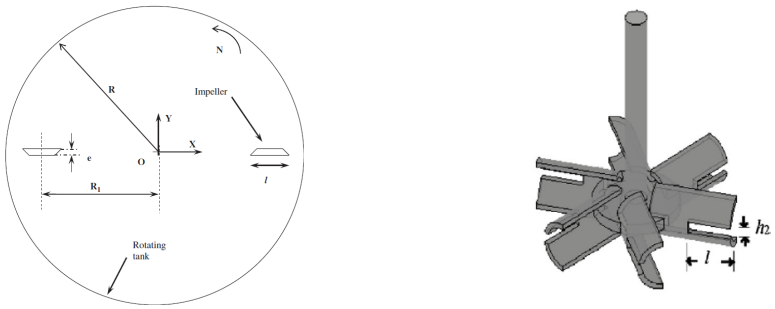

(a) (b)

Figure 1.5: (a) The top view of geometry used by Savreux et al. (2007); (b) Impeller used by Ameur and Vial (2020).

their experiments showed that increasing rotational speed was not sufficient to reduce the volume of dead zones.

1.5.2 The effect of the vessel and impeller design

Ameur and Vial (2020) created some cuts on blades of a Scaba 6SRGT impeller (illustrated in Fig. 1.5b) to investigate the effects of height of cuts, length of cuts, and the number of cuts on the flow field and power consumption, numerically. They found increasing the height of cuts height, cuts length, and the number of cuts reduced the power consumption. However, the cavern size decreased as a result of increasing the surface area of cuts. In another work, Ameur (2020) introduced some holes with different shapes and sizes on blades of a Scaba 6SRGT impeller. A circular hole

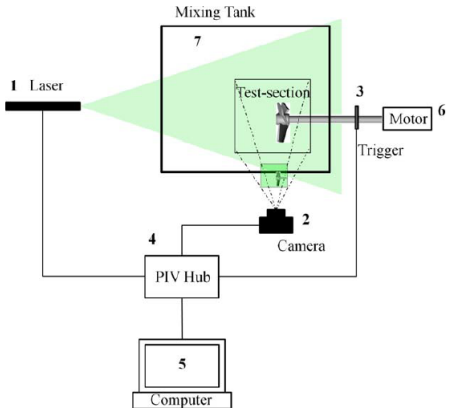

Figure 1.6: Experimental setup used by Sossa-Echeverria and Taghipour (2014).

was more successful to reduce the power consumption compared to the lozenge-shaped, rectangular, and triangular holes. Arratia et al. (2006) used both experimental and numerical tools to investigate the mixing of non-Newtonian fluids with yield stress in a cylindrical tank equipped with Rushton impellers. They found that by displacing the impeller shaft from the center, axial component velocities improved and better mixing occurred between caverns. Sossa-Echeverria and Taghipour (2014) conducted experiments to investigate the effect of impeller type, vessel shape (cylindrical and rectangular), and clearance (a distance between the side wall and the impeller) on the flow field in a stirred tank equipped with side-entry impellers (Figure 1.6). The fluid used was a yield stress fluid. They defined the cavern as the region where the velocity magnitude exceeds 2 % of impeller tip velocity. Results showed that the cavern was larger in a rectangular vessel. Ameur (2016a) numerically studied an unbaffled cylindrical vessel equipped with two six-curved bladed impellers to characterize the mixing of xanthan gum solution (Figure 1.7a). The location of impellers was not centric. They found that when two impellers are at the same level, larger dead zones are created. Ameur et al. (2015) used CFD tools to study velocity field and power consumption in a stirred tank filled with a xanthan gum solution. They considered a stirred tank with three Scaba 6SRGT impellers on the shaft (Figure 1.7b). Toroidal vortices between impellers were seen. In addition, they found by increasing the vessel diameter, more rigid zones were observed. In another work (Ameur, 2016b), they examined the effect of the shape of bottom wall of the vessel on the flow field and energy consumption. They found that for a closed spherical vessel, less energy was needed to mix

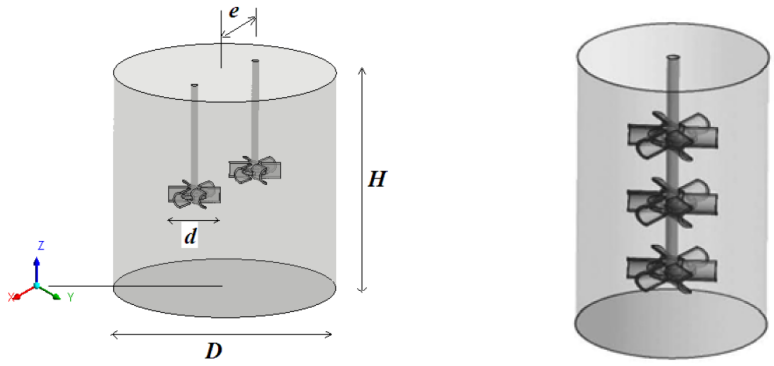

(a) (b)

Figure 1.7: Impeller configurations used by (a) Ameur (2016a); (b) Ameur et al. (2015).

the same amount of fluid compared to other vessel designs (flat and dished bottomed cylindrical vessel). Prajapati and Ein-Mozaffari (2009) used numerical simulations to study the 3D flow field of mixing of viscoplastic fluids. They considered the effect of impeller geometry on the mixing time and power consumption. By analyzing the mixing time and power consumption, it was found that a four-blade anchor impeller was more efficient than a two-blade anchor impeller. Ein-Mozaffari and Upreti (2009) investigated the effect of geometrical parameters, such as impeller types and clearance (a distance between bottom wall and the impeller) on the mixing of xanthan gum solutions. CFD modelling showed that at higher clearances, the mixing time decreased. Also, their results showed that using A310 impeller reduced the mixing time in comparison with pitched blade turbine and marine impellers. Kazemzadeh et al. (2017) used different configurations of impellers in a stirred tank to study the mixing of a homogeneous viscoplastic fluid, both experimentally and numerically (Figure 1.8). They found that Scaba-pitched blade-anchor coaxial impellers (illustrated in Fig. 1.8b) were more efficient compared to other configurations because the mixing time decreased. The mixing performance of a yield stress fluid in a coaxial mixer was evaluated both experimentally and numerically by Pakzad, Ein-Mozaffari, Upreti, and Lohi (2013a). They combined an anchor impeller and a Scaba impeller (the same geometry used by Kazemzadeh et al. (2016)). The effect of anchor impeller speed and Scaba impeller speed on the mixing time and power consumption was examined. They also considered the effect of two operation modes: co- and counter-rotating modes. Results showed that more power consumption and mixing time resulted when the counter-rotating mode is used. A. Russell et al. (2020) examined the effect of impeller arrangement on the flow

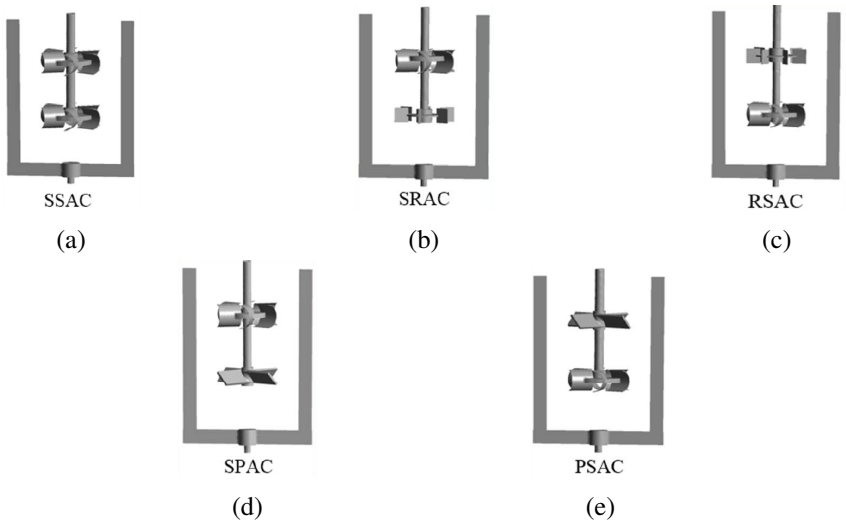

Figure 1.8: The side view of impeller configurations used by Kazemzadeh et al. (2017) (a) Scaba-Scaba-anchor (SSAC); (b) Scaba-Rushton-anchor (SRAC); (c) Rushton-Scaba-anchor (RSAC); (d) Scaba-pitched blade-anchor (SPAC); (e) pitched blade-Scaba-anchor (PSAC).

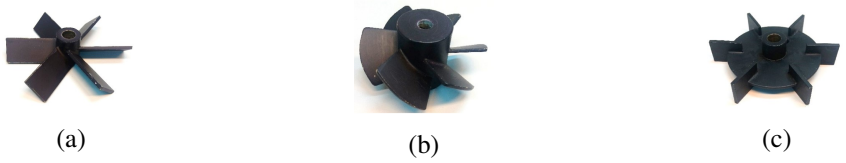

Figure 1.9: Tested impellers used by Story et al. (2021) (a) Pitched blade turbine; (b) Prochem Maxflo T; (c) Rushton turbine.

behavior both experimentally and numerically. A combination of two kinds of impellers (RT and PBT) was used. A better mixing, in terms of homogeneity and power consumption, was seen when the PBT (upper)-RT (lower) configuration was used. Story et al. (2021) investigated the effect of impeller type on the tangential force which is calculated from the measured torque. Pitched blade turbine, Prochem Maxflo T, and Rushton turbine were used (Figure 1.9). Their results showed that Prochem Maxflo T exerted more tangential forces. Four different geometries were used by Benhanifia et al. (2022) to investigate the mixing of viscoplastic fluids (Figure 1.10). They found that all geometry configurations show the same power consumption rate during the mixing process.

The existing literature predominantly focuses on studying the impact of rheological parameters and geometry on mixing characteristics in a dimensional form (without employing dimensionless numbers to characterize the problem). For instance, Pakzad et al. (2008a) discovered that higher

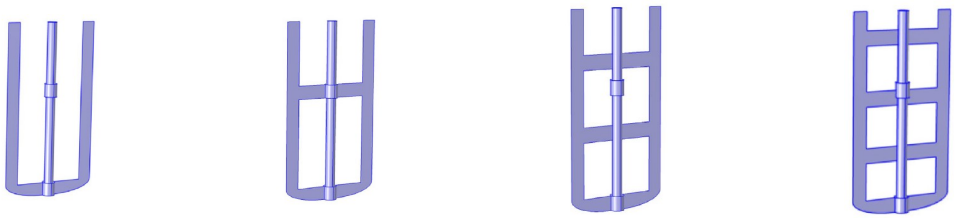

(a) (b) (c) (d)

Figure 1.10: Tested impellers used by Benhanifia et al. (2022) (a) Classical anchor impeller; (b) Anchor impeller with added horizontal arm blade; (c) Anchor impeller with two blades; (d) Anchor impeller with three blades.

yield stress leads to increased mixing time. However, this approach presents challenges when attempting to establish connections between the findings of different studies. Conversely, dimensionless analysis enables the comparison and characterization of similar phenomena across diverse systems and scales. Some researchers (Burghelea, 2023; Pakzad et al., 2013a; A. W. Russell et al., 2019) have formulated the problem based on the following dimensionless numbers (Reynolds and Bingham numbers).

$$Re = \frac{\hat{\rho}\hat{\Omega}\hat{D}^2}{\hat{\mu}_p} \tag{10}$$

$$Bn = \frac{\hat{\tau}_y}{\hat{\mu}_p\hat{\Omega}} \tag{11}$$

We know from the celebrated paper of Reynolds (Reynolds, 1883), one of the main roles of Reynolds number is to determine whether inertia is negligible or dominant. However, in this kind of definition, Reynolds number values do not show whether the inertia effect is dominant or not (Thompson & Soares, 2016). Because yield stress (plastic behavior) is absent in the definition of Reynolds number. For example, it is possible that the value of Reynolds number is large, however, the inertia is not dominant because Bingham number is large as well. Consequently, it is crucial to adopt a novel approach to derive dimensionless numbers, which can lead to fresh insights and potentially yield new results. Further details regarding this approach will be discussed in the subsequent sections.

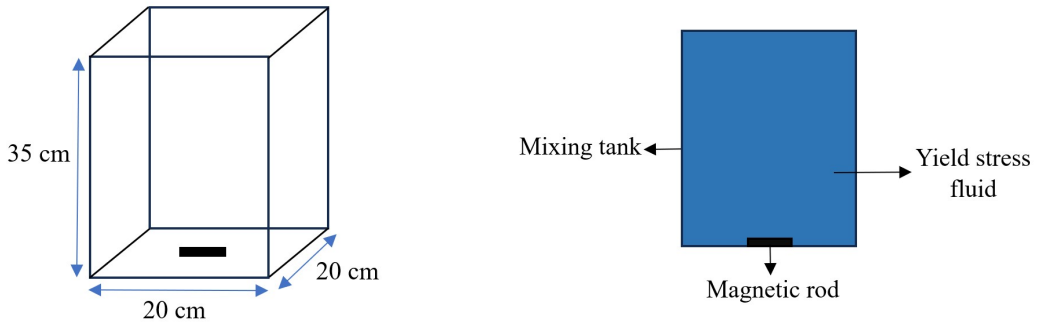

Figure 1.11: (a) Three-Dimensional schematic of the model; (b) Two-Dimensional schematic of the model.

1.6 Problem setup

We conduct an experimental research on the mixing in a rectangular mixing tank shown in figure 1.11. Details of the experimental apparatus are presented in chapter 2. A rectangular tank was chosen because the cavern won't extend to the walls. Additionally, conducting PIV in a rectangular tank is easier compared to a circular tank where light distortion occurs. Also, due to the cavern not reaching the walls, the influence of the walls is not taken into account in this study. The tank is filled with a simple yield stress fluid (Carbopol solution) and a magnetic stirrer with a cylindrical rod is used to promote mixing.

Creating a dimensionless number that quantifies the interaction between inertial and frictional forces allows for a more effective characterization of flow behavior and yields novel insights and outcomes (Blackwell, Deetjen, Gaudio, & Ewoldt, 2015; Nirmalkar, Chhabra, & Poole, 2013). In the current study, the characteristic inertial stress ($\hat{\rho}\hat{\Omega}^2\hat{D}^2$) and frictional stress ($\hat{\tau_y} + \hat{K}\hat{\Omega}^n$) are used to define a dimensionless number (equation 12) to be able to measure the competition between inertia and frictional effects. By consolidating all the resistant forces (plastic and purely viscous forces) into a single dimensionless number, the competition between inertial and frictional forces provides a clearer understanding of the fluid flow dynamics (Thompson & Soares, 2016).

$$Re = \frac{\hat{\rho}\hat{\Omega}^2\hat{D}^2}{\hat{\tau_y} + \hat{K}\hat{\Omega}^n} \tag{12}$$

Also, AR is a geometrical dimensionless number (equation 13) that expresses the ratio of the rod's diameter (D) to its thickness (b).

$$AR = \frac{\hat{D}}{\hat{b}} \tag{13}$$

Totally, the problem is governed by four dimensionless numbers, which are mentioned below. The impact of all the listed numbers could not be observed because altering one of them while maintaining the others simultaneously was not possible.

$$(\frac{\hat{\rho}\hat{\Omega}^2\hat{D}^2}{\hat{\tau_y} + \hat{K}\hat{\Omega}^n}, \frac{\hat{\tau_y}}{\hat{\tau_y} + \hat{K}\hat{\Omega}^n}, n, \frac{\hat{D}}{\hat{b}}) \tag{14}$$

1.7 Research goals

In the previous section, a dimensionless number, denoted as Re, was introduced to quantify the competition between the inertial and frictional forces. Consequently, the following questions can be identified as research gaps that will be addressed in this work.

- How do the stirring characteristics, such as cavern size and velocity norm change as Re increases? How can different values of Re impact the mixing process, particularly when inertia becomes more dominant?
- How does the shape of the cavern change as the value of Re increases? Is the position of the rod affecting the boundaries of the cavern?
- According to the literature, there are two primary criteria used to define the boundaries of the cavern: velocity and concentration fields. Is the shape of the cavern similar when utilizing velocity and concentration criteria to determine the boundaries of the cavern (at the same condition)?

Chapter 2

Experimental setup and methodology

The Experimental Setup and Methodology section provides a comprehensive description of the procedures and equipment used to conduct the research. This section outlines the systematic approach taken to ensure the reliability and accuracy of the experimental data. The experimental setup was carefully designed to address the research objectives and answer the research questions.

The section begins by detailing the selection and preparation of the research materials, including any samples, specimens, or data sources used. Next, the instrumentation and equipment utilized in the research are described. This includes providing information about the specific instruments, tools, or devices employed, along with their manufacturers, models, and technical specifications. The experimental procedures are then outlined in a step-by-step manner.

2.1 Fluid preparation and properties

2.1.1 Fluid preparation

In this section, the process of Carbopol preparation is discussed. Carbopol is commonly used in various industries and has a wide range of applications (Lubrizol, 2010). Carbopol-based gels are highly convenient for conducting chemical and experimental studies. Their user-friendly nature simplifies the process, making them ideal for various research purposes. The ease of use associated with these gels proves advantageous when performing experiments and analyzing results in a laboratory setting. Their versatility and suitability for experimentation make them a preferred choice for

scientific investigations. Experimental studies on these gels indicate that upon neutralization, they develop yield stress (Di Giuseppe et al., 2015; Lubrizol, 2010; R. Varges, M. Costa, S. Fonseca, F. Naccache, & de Souza Mendes, 2019). Lubrizol conducted rheological characterization and flow properties analysis, which revealed that these gels demonstrate significant yield values that vary based on the concentration of the polymer. (Lubrizol, 2010). Due to their significant yield values and versatile rheological properties, Carbopol gels have emerged as one of the most widely utilized yield stress fluids in fluid mechanics research (Di Giuseppe et al., 2015; R. Varges et al., 2019). Carbopol ETD2050 NF powder is used to prepare our samples.

The procedure for preparing Carbopol gels involves the following steps.

- Take 4000 ml of distilled water in the 5-liter glass beaker.
- Measure the desired amount of Carbopol powder using a digital balance.
- Start mixing the water in the beaker at about 600RPM using a mechanical stirrer.
- Add Carbopol slowly to water to avoid lumps while mixing at 600RPM.
- Increase the mixing rate to about 800RPM. Allow the solution to mix for about 30 min.
- Set the rotational speed of mixer at 50 rpm and start mixing. Use 5M NaOH solution to neutralize the Carbopol water mixture. Use a micropipette to slowly add NaOH in amounts of about 100 microliters increments.
- Change the location of impeller (top, middle, and bottom of the tank) and allow 5 minutes at each location between increments before testing pH to ensure proper mixing (Also, increase the mixing quality by making the impeller off-center by displacing the tank).
- Add NaOH until the solution becomes neutral (pH=7). At this point, you can observe a gelled solution.

It is essential to wear personal protective equipment, including nitrile gloves, lab coats, and safety glasses, throughout the entire preparation process. Extra caution should be exercised when adding NaOH to the solution.

2.1.2 Rheological characterization

For measuring the rheological characteristics of Carbopol gels, a hybrid DHR20 TA rheometer was employed. We utilized a parallel plate geometry with a diameter of 40mm and a 1mm distance between the plates. Rheology tests were conducted using the stress-strain ramp method to determine the yield stress. In the stress-strain ramp method, a range of strain rates is systematically applied to the material, gradually increasing from low to high values, resembling a ramp. The resulting data is then used to fit various models that enable the prediction of the material's yield stress. The steps involved in rheological experimentation can be outlined as follows:

- The rheometer is equipped with a parallel plate geometry that is used to mount the gel sample. This parallel plate geometry consists of two plates, with one plate serving as the stationary lower plate and the other as the movable upper plate.

- The gel sample is carefully placed on the lower plate, ensuring proper contact and alignment between the plates.

- Once the gel sample is mounted, the upper plate, which is connected to the motor shaft, is incrementally moved towards the bottom plate to maintain a consistent plate gap difference of 1mm. It is important to carefully control the advancement to prevent any spillage or leakage of the sample through the gap between the plates.

- The stress-strain ramp method is utilized for conducting the experiments. In the software, the experimental conditions are set according to the desired parameters. The experiments are performed at a controlled room temperature of 24 degrees Celsius. This temperature is maintained throughout the duration of the experiments to ensure consistent and reproducible results.

- For the experiments, a range of strain rates was selected, spanning from 10^{-3} to 100 s^{-1}. This range allows for the investigation of the gel's response at various deformation rates. The experiments were conducted over a duration of approximately 2 minutes, during which the gel's rheological behavior was measured and recorded at different strain rates within the specified range.

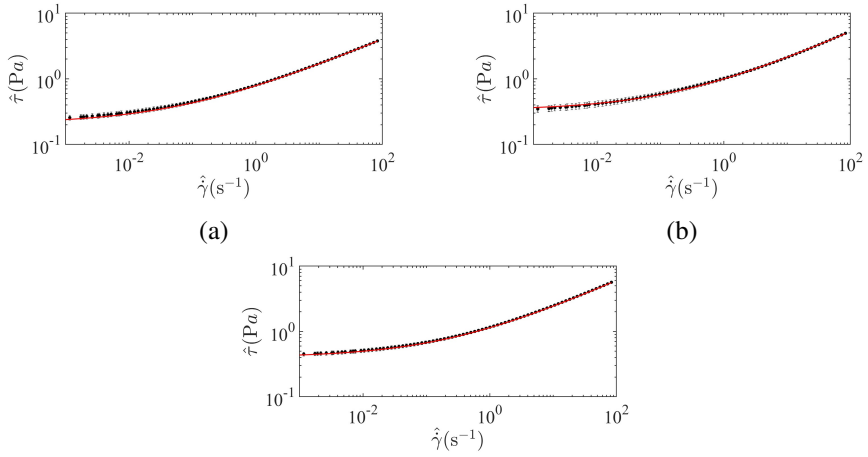

Figure 2.1: Flow curves of Carbopol solutions (a) concentration of 0.35 g/L; (b) concentration of 0.4 g/L; (c) concentration of 0.45 g/L. The circle markers show the measured flow curved, averaged over multiple tests. The error bars indicate the standard deviation of the measurements. The red line shows the fitted Herschel-Bulkley model.

- In order to assess repeatability, the aforementioned steps were repeated for each concentration of Carbopol gel being tested.

Based on the calculation, the maximum angular velocity inside the tank is equal to 68 s^{-1}. We used this value to estimate the upper limit of the strain rate (100 s^{-1}) to perform rheology tests. Repeatability tests were conducted using multiple samples of Carbopol gels across all concentrations. In our presentation of the data (figure 2.1), we include error bars that represent the standard deviation of the mean. It is important to note that the error associated with the standard deviation of the mean was found to be relatively small for all the measured experimental data points. Herschel-Bulkley model was fitted to the flow curves to find the rheological properties. More details about the flow curves and rheological properties can be found in figure 2.1 and Table 2.1.

2.2 Experimental setup

A transparent acrylic rectangular stirred tank, as depicted in figure 2.2a, is utilized for the experiment. The cross section is a square with a length of 20 cm. The height of container is 35 cm. A magnetic stirrer (OHAUS Inc, STLC1DG) is used to promote mixing. The angular velocity ranges

Table 2.1: Physical and rheological properties of Carbopol solutions used in this work.

Cases	Concentration (g/L)	pH	Yield stress, τ_y (Pa)	Flow consistency, K (Pa.s^n)	Power-law index, n
Fluid 1	0.35	7	0.22	0.58	0.41
Fluid 2	0.4	7	0.33	0.66	0.44
Fluid 3	0.45	7	0.41	0.75	0.44

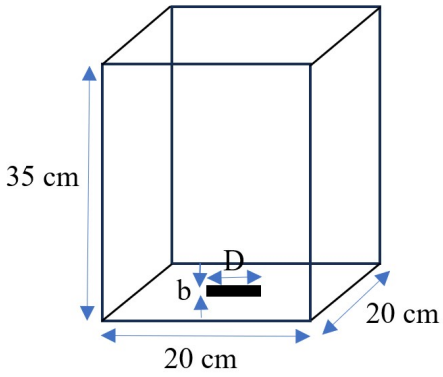

(a)

(b)

Figure 2.2: (a) The layout of the stirred tank configuration equipped with the magnetic rod (b) Photo of stirring bars used in this research.

from 100 to 1500 rpm. The shape of stir bar is cylindrical with a specific length (D) and thickness (b). In this work, two rods with the same thickness and a length of 1.9 and 3.8 cm are used (figure 2.2b).

2.3 Measuring techniques

This study employs two distinct measurement techniques, namely Particle Image Velocimetry (PIV) and Dye Visualization. The subsequent sections provide a more comprehensive description of these methods.

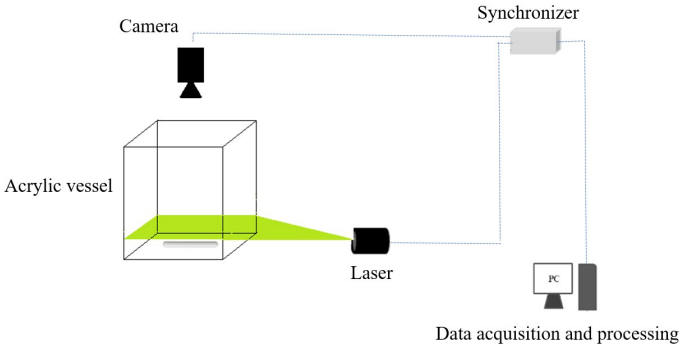

Figure 2.3: The schematic of the PIV experimental setup.

2.3.1 Particle Image Velocimetry

We utilize Particle Image Velocimetry (PIV) as a non-intrusive optical technique to acquire the velocity field in this study. The experimental setup for planar PIV is illustrated in figure 2.3. The setup comprises a 532 nm Nd-Yag laser (Litron Laser, 15 Hz, 800 mJ), a high-speed camera (Flowsense M2) with a spatial resolution of 2 MP, a synchronizer box, and an acquisition system. The measurement plane is consistently positioned 1 cm above the bottom wall for all cases. Polyamide seeding particles (PSP) with a diameter of 50 μm are employed in the PIV measurements. Further information regarding the PIV system can be found below.

- Pulsed laser: We utilize a 532 nm (Nd:YAG) laser that operates with double beams and a frequency of 30 microseconds. The laser controller enables us to adjust the laser energy output as needed. The pulsed laser emits radiation in short bursts. The laser controller is equipped with inputs for the laser head, camera, and synchronization unit. Additionally, it includes a monitor that allows us to control all the hardware using specialized software.

- Cylindrical lens: This optical device is designed to transform a highly concentrated laser beam into a light sheet. The optical head is connected to a diverging lens, which separates the beam into a sheet-like structure. The laser sheet is then used to illuminate the cross-sectional area of a flow field. Working with light sheets is generally considered safer compared to using laser beams, as there is a reduced risk of reflections and associated hazards.

- Camera: For capturing the illuminated flow field, we utilized a Dantec Dynamics Flowsense

M2 camera. This camera is equipped with CCD (charged coupled device) chips, which contribute to improved image quality. It offers a pixel resolution of up to 1200x1600 pixels, ensuring detailed and high-resolution images. With a quantum efficiency of 70 percent and a dynamic range of 12 bits, the camera provides excellent sensitivity and the ability to capture a wide range of brightness levels in the flow field.

- Flowmanager: The Flow Manager software serves as the control hub for image acquisition and the management of various hardware components. Once all the devices are connected, the software enables us to specify the desired laser and camera frequency for capturing images at regular intervals. After configuring the timing settings, we can use the preview function to view the live image feed. It is important to note that we exclusively utilized this software for image acquisition purposes. For post-processing tasks, we employed PIVlab software (Stamhuis & Thielicke, 2015), which will be discussed in more detail later.

In the following, the experiment procedure is described.

- Make sure the Carbopol gel inside the mixing tank is free of air bubbles.
- Make sure the magnetic stirrer is plugged in.
- Verify the connections of the camera and ensure that it is oriented towards the laser sheet that is aligned horizontally.
- Switch off the lighting. Conduct experiments against a backdrop with low light conditions.
- Activate the laser while adhering to laser safety protocols. Ensure that the laser sheet is maintaining a horizontal alignment. Take precautions to eliminate any reflections in the laser sheet.
- Configure the software to accommodate the desired number of tests to be performed. Set the acquisition frequency of the laser to the desired rate for data collection.
- Create a project folder and name it with the current date and the concentration of Carbopol used, specifically for storing the test images.

- Prior to commencing image acquisition with the laser, perform camera calibration to establish a conversion factor from pixels to length units. Place the calibration target within the flow field and capture an image of it. Utilize the software's "show preview" feature to view live images.
- Begin the process of image acquisition by pressing the "Initialize Acquire" button for the first test.
- Turn on the mixer.
- After each test, remember to save the captured images for analysis once the experiments are complete.
- Reinitialize the image acquisition by resetting the settings for the next test. Set the desired number of pictures to be taken during the upcoming test.
- Create a backup copy of the test results by copying them to an external hard drive for safe-keeping.

We utilize PIVlab, an add-on application integrated within MATLAB, for data analysis and post-processing purposes. PIVlab offers a user-friendly and efficient solution for determining velocities within flow fields. Its key features encompass image sequencing, applying filters for image pre-processing, selecting regions of interest (ROI), image calibration, validating velocity vectors, and deriving results such as streamlines, velocity magnitude, and vortices. PIVlab serves as a powerful tool, employing cross-correlation techniques, and is equipped with a graphical user interface integrated into MATLAB for initiating the post-processing software. The post-processing workflow in PIVlab can be broadly categorized into three steps: Image pre-processing, Image Evaluation, and Post-processing.

Image pre-processing

The software loads the images based on the desired cross-correlation time ($\hat{t}_{cc}$). The cross-correlation time refers to the time interval between two successive images that is used to calculate the velocity field. Once the images are loaded, the software performs sequencing of image pairs

for image evaluation. The sequencing can be done in a sequential manner, such as 1-2, 2-3, 3-4, or 1-2, 3-4, 5-6. The sequenced image pairs are then imported into the solution window for further processing. Following image import, the software allows the selection of a region of interest (ROI) to exclude unwanted areas of the image. Additionally, the images are calibrated by entering the actual size of the calibration target and the time interval between image pairs as calibration parameters.

Image Evaluation

Once the calibration process is complete, the software applies the Fast Fourier Transform (FFT) technique to all the imported images in order to determine the velocity. Each interrogation window has an area of 32 by 32 pixels (for all analyses). The multi-pass PIV evaluation method with the interrogation size of 128, 64, and 32 and an overlap of 50% is used.

Post-processing

To ensure the accuracy of the final velocity data, a data validation step is performed, which involves removing unwanted velocities or outliers that are deemed irrelevant. Additionally, smoothing techniques are applied to eliminate noise from the data. Once this validation and smoothing process is complete, the PIV problem is effectively solved. At this stage, various results can be explored, including velocity magnitude, streamlines, vorticity, and other flow field features that can be extracted. The software allows for the export of a text file containing the solution, which includes the velocity components of each vector distributed within the flow field.

Thompson τ technique (Wheeler, Ganji, Krishnan, & Thurow, 2010) was used to filter the experimental data, e.g., in characterizing the cavern area. In this method, the mean ($\bar{\hat{x}}$) and standard deviation ($\hat{S}$) of the data points are calculated. The maximum and minimum values are potential outliers. To make sure, the deviation of these values from the mean value is calculated.

$$\hat{\delta}_i = |\hat{x}_i - \bar{\hat{x}}| \tag{15}$$

The largest value of this deviation is compared with the product of τ and standard deviation ($\tau\hat{S}$). If $\hat{\delta}_i$ is larger than $\tau\hat{S}$, this data point can be considered an outlier. This process is repeated until no data point is eliminated.

• **Cross-correlation time selection**

The procedure of the cross-correlation time selection is discussed. According to PIV references (Adrian & Westerweel, 2011; Raffel, Willert, Kompenhans, et al., 1998), to increase the accuracy of results, the displacement of seeding particles between two successive recordings should be less than a quarter of the interrogation window size. According to this rule, the time interval can be calculated based on the maximum velocity and the size of the interrogation window. The maximum velocity occurs at the tip of the impeller. According to PIV studies on flows in stirred tanks (Bugay, Escudié, & Liné, 2002; Myers, Ward, & Bakker, 1997; Zalc, Alvarez, Muzzio, & Arik, 2001), the fluid velocities range from 20 to 52 percent of the tip velocity in the vicinity of the impeller. Therefore, an experiment plan was designed to investigate the cross-correlation time value on the flow field.

According to this plan, a four-liter Carbopol solution was used (the rheological properties in Table 2.1) and the rod with a length of 1.9 cm and a thickness of 7.9 mm was chosen. In this section, the angular velocity of the rod is 300 rpm in all experiments and the measurement plane is 1 cm above the bottom wall. Data are collected at the steady-state condition and PIV images are captured after five minutes after the onset of the rod. The interrogation window size is 0.00544 m and the velocity of the rod's tip (maximum velocity) is 0.3 m/s. Hence, the cross-correlation time is calculated as.

$$\Delta\hat{t} = \frac{\Delta\hat{x}}{\hat{V}} \tag{16}$$

where $\Delta\hat{x}$ and $\hat{V}$ are the displacement of particles between two consecutive images and velocity magnitude, respectively. The displacement ($\Delta\hat{x}$) is equal to 0.00136 m (a quarter of the interrogation window size). The cross-correlation time used to measure the flow field was from 4500 to 30000 microseconds. The first criterion which helps to determine the suitable cross-correlation time is the number of spurious vectors. One common method used to identify and eliminate the spurious vectors is the median test (Raffel et al., 1998). In simpler terms, median filtering in PIV involves sorting neighboring velocity vectors based on their magnitudes or individual components. The middle value in this sorted list, which is the fourth or fifth value out of eight neighbors, is considered the median value. To determine the validity of a velocity vector, we calculate the difference between

Table 2.2: Percentage of spurious vectors for each cross-correlation time

Cross-correlation time (μs)	Percentage of spurious vectors (%)
4500	0.65
7000	1.31
10000	1.76
12000	1.83
13000	2.89
14000	2.76
15000	3.12
16000	2.86
17000	4.58
18000	4.32
19000	4.73
20000	5.67
25000	6.90
30000	7.34

the vector under examination and the median vector. If this difference is below a certain threshold, the velocity vector is considered valid. By applying this test, the number of spurious vectors is detected for each experiment. The results are given in Table 2.2.

Results show that the cross-correlation of 4500 (μs) is more suitable. Also, in the measurement plane, by increasing the distance from the rod, the velocity decreases. This means selecting a higher cross-correlation time helps to capture the displacement of particles located far from the rod. Here, the second criterion comes into the picture, the root-mean-square (rms) deviation (Raffel et al., 2018). To examine this criterion, the steady velocity norm is calculated for each experiment.

$$||\hat{u}|| = \sqrt{\iint |\hat{V}|^2 \, d\hat{x} d\hat{y}} \tag{17}$$

$\hat{V}$ is the velocity magnitude of each interrogation window. The variation between the steady-state velocity norm of the suitable cross-correlation time (selected from the previous criterion) and other cross-correlation times is quantified by calculating the rms deviation.

$$\text{rms} = \frac{[\frac{1}{N}\sum_{i=1}^{N}(||\hat{u}||_{(\hat{t}_{cc})_1} - ||\hat{u}||_{(\hat{t}_{cc})_2})^2]^{\frac{1}{2}}}{[\frac{1}{N}\sum_{i=1}^{N}(||\hat{u}||_{(\hat{t}_{cc})_2})^2]^{\frac{1}{2}}} \tag{18}$$

Table 2.3: The rms deviation for each cross-correlation time

Cross-correlation time (μs)	The rms deviation (%)
7000	13.15
10000	19.32
12000	9.86
13000	12.69
14000	19.77
15000	18.74
16000	9.19
17000	20.93
18000	20.69
19000	17.36
20000	21.61
25000	25.89
30000	30.15

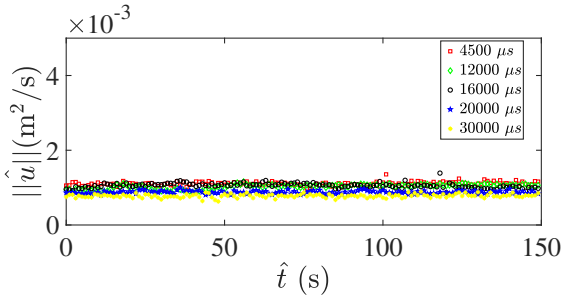

Figure 2.4: The steady-state velocity norm for various cross-correlation times.

The rms deviation values are summarized in Table 2.3. Also, the steady-state velocity norm values of different cross-correlation times are shown in figure 2.4. According to these results, the rms of the cross-correlation time of 16000 μs is less than other cases. Hence, this cross-correlation time was chosen to perform experiments when the angular velocity is 300 rpm. By assuming the proportional relation, the cross-correlation time is obtained for other angular velocities.

2.3.2 Dye Visualization

Dye visualization has been employed as a technique to characterize caverns within viscoplastic fluids. This method involves injecting a small volume of ink near the impeller prior to initiating the experiment (Amanullah et al., 1997; A. W. Russell et al., 2019). As the stirring process commences,

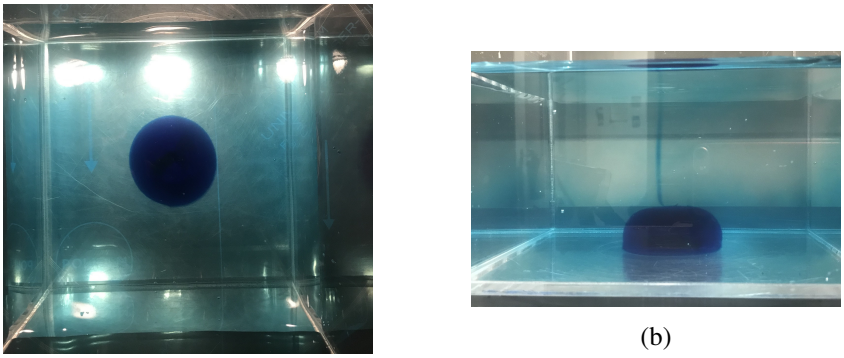

(a) (b)

Figure 2.5: Colorful shape formed around rod after dye injection at $Re = 800$ (a) Top view; (b) Side view.

the ink spreads throughout the vessel, resulting in the formation of a colored region surrounding the impeller. Over time, this colored region tends to expand before reaching a stable shape. The final steady shape of the colored region is typically recognized as the cavern.

A low angular velocity is set initially and 1 or 2 mL of blue food dye is injected at the rod tip. Then, the angular velocity is incrementally increased. At each rotational velocity, images are taken (iPhone 7 camera) after 5 minutes to allow the cavern to attain an equilibrium size and shape. Figure 2.5 shows an example of images taken from top and side views. RGB images are converted to grayscale images by using MATLAB codes and each pixel corresponds to a single value representing the brightness of the original RGB pixel. Hence, the intensity field is obtained for each image.

2.4 Motionless state characterization

To distinguish the motionless state from the systematic motion, a velocity threshold is introduced in this section. Image pairs, captured under the same conditions as described earlier, are obtained when the solution is motionless. These image pairs are acquired at different cross-correlation times, meaning that the time interval between consecutive images varies while the fluid remains stationary. The image pairs are analyzed and velocity vectors are obtained for each interrogation area. The average velocity vectors in x and y directions ($\bar{\hat{u}}$ and $\bar{\hat{v}}$) for each image pair are calculated.

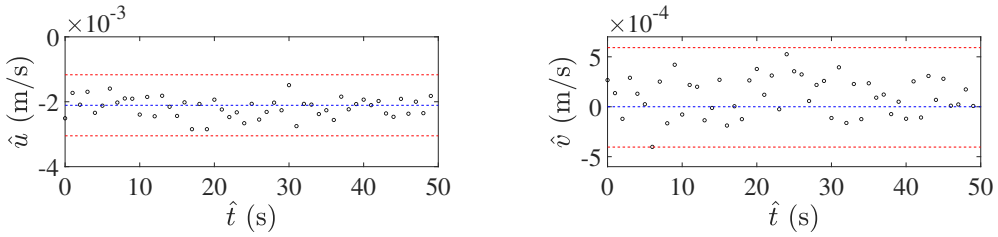

(a) (b)

Figure 2.6: The evolution of velocity for the motionless fluid (a) x-component of velocity; (b) y-component of velocity. Dashed blue and red lines show the average and upper and lower bounds, respectively.

$$\bar{\hat{u}} = \frac{\int \hat{u} d\hat{A}}{\hat{A}} \tag{19}$$

$$\bar{\hat{v}} = \frac{\int \hat{v} d\hat{A}}{\hat{A}} \tag{20}$$

$\hat{u}$ and $\hat{v}$ are x-component of velocity and y-component of velocity in each interrogation area. $\hat{A}$ is the area of domain. For each cross-correlation time, 50 image pairs are analyzed and average velocity is obtained. Then, the upper and lower bounds with a confidence level of 99 percent are obtained.

$$\hat{P}_{\bar{x}} = \pm \frac{t\hat{S}_x}{\sqrt{n}} \tag{21}$$

$$\hat{S}_x = (\sum_{i=1}^{N} \frac{(\hat{x}_i - \bar{\hat{x}})^2}{n-1})^{1/2} \tag{22}$$

$\hat{P}_{\bar{x}}$, n, and $\hat{S}_x$ are uncertainty, number of samples, and standard deviation, respectively. The value of t can be obtained using the reference (Wheeler et al., 2010). As an example, the upper and lower bounds for $\hat{u}$ and $\hat{v}$ are shown in figure 2.6 when the cross-correlation time is 4 ms. When the value of $\hat{u}$ and $\hat{v}$ is outside of this range, systematic motion occurs.

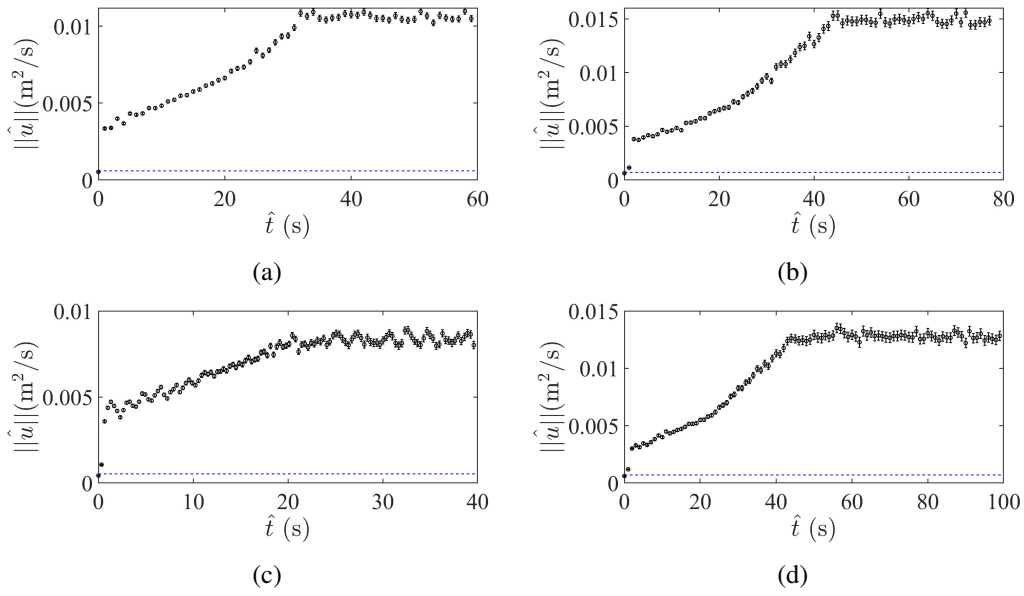

Figure 2.7: (a) Error bar for 0.4 g/L, rod length of 3.8 cm, and angular velocity of 500 rpm; (b) Error bar for 0.4 g/L, rod length of 3.8 cm, and angular velocity of 600 rpm; (c) Error bar for 0.35 g/L, rod length of 3.8 cm, and angular velocity of 400 rpm; (d) Error bar for 0.45 g/L, rod length of 3.8 cm, and angular velocity of 600 rpm. The dashed blue line marks the distinction between the systematic movement and the stationary state.

2.5 Repeatability tests

To ensure the reproducibility of the results, repeatability tests were carried out. Figure 2.7 illustrates the standard deviation of velocity norms at each point. The experiments were repeated for various concentrations and different angular velocities. Notably, the standard deviation in the mean of the instantaneous velocity norm remained sufficiently low throughout all time intervals for every concentration.

Chapter 3

Results and discussions

3.1 Flow development

In this section fluid flow development is discussed. Figure 3.1 depicts the flow development concerning the longer rod ($L = 3.8cm$) at an angular velocity of 400 rpm. Figure 3.1a and 3.1b depict the progression of angular velocity and velocity norm as the rod initiates its rotation. It can be observed that the instantaneous angular velocity and the velocity norm exhibit a similar development pattern. The velocity norm plot shows two distinct phases. In the first phase, there is a sharp jump in the velocity norm for all cases. This jump is likely due to the initial acceleration of the fluid caused by the rotation of the rod. In the second phase, a more gradual and smooth behavior is observed until the system reaches a steady-state condition which is in consistent with the development of angular velocity. Figures 3.1c to 3.1h display snapshots of the velocity field, clearly demonstrating that increasing the instantaneous angular velocity results in greater magnitudes of maximum velocity within the flow field.

Figure 3.2 presents the evolution of the velocity norm at different concentrations and angular velocities. Based on the rheology tests, an increase in concentration leads to an increase in yield stress and consistency. The figure indicates that with an increase in both yield stress and consistency, there is a decrease in the velocity norm. Additionally, similar to previous findings, the development of the velocity norm develops in two distinct stages.

Figures 3.3, 3.4, and 3.5 illustrate the development of the systematically flowing area (denoted

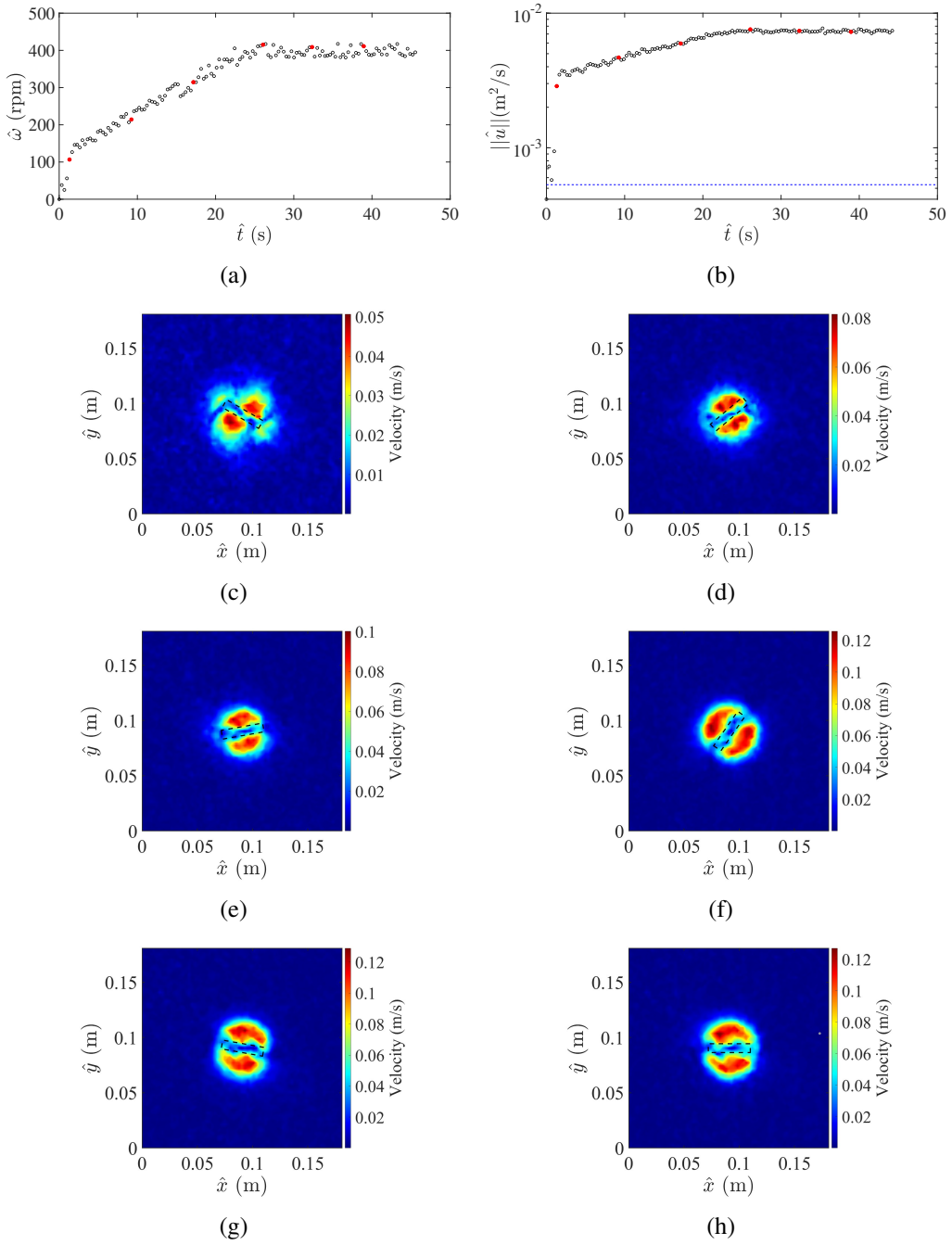

Figure 3.1: Illustration of (a) the angular velocity evolution (b) the velocity norm evolution at angular velocity of 400 rpm and rod length of 3.8 cm (c,d,e,f,g,h) snapshots of the velocity field. The red circles in 3.1a and 3.1b indicate the times when the snapshots are taken. The dashed blue line in 3.1b marks the distinction between the systematic movement and the stationary state. The dashed black line shows the position of the rod. The fluid properties are: $\hat{\tau_y} = 0.33$ Pa, $\hat{K} = 0.66$ Pa.s$^{\text{n}}$, and $n = 0.44$.

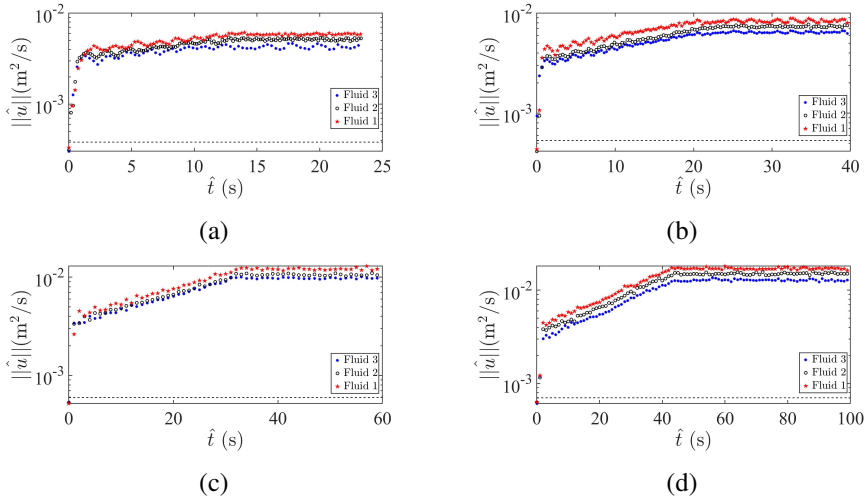

Figure 3.2: The evolution of velocity norm for different fluid cases, rod length of 3.8 cm and angular velocities of (a) 300 rpm; (b) 400 rpm; (c) 500 rpm; (d) 600 rpm.

as $\hat{A}_{motion}$) at various angular velocities. Outside systematically flowing region, we can be confident at a 99% confidence level that there is no systematic motion (more details in section 2.4). Based on these figures, $\hat{A}_{motion}$ initially decreases and subsequently increases until it reaches a steady-state condition. It's important to note that the rod's rotation is clockwise. The velocity vector maps at different time instants reveal the coexistence of both clockwise fluid motion (enclosed by red dashed lines) and counterclockwise fluid motion (enclosed by blue dashed lines) with respect to the center of the tank. As time progresses, the area of the counterclockwise motion zones diminishes, which explains the initial decreasing trend observed in $\hat{A}_{motion}$.

3.2 Flow stoppage

To study how energy decays in the fluid, the mixer is turned off a short while after the flow reaches a periodic steady-state. To determine the point at which the transient mode begins, the upper and lower bounds of the steady data points are calculated with a 99% confidence level. Figure 3.6 provides an example of this process. The first data point that falls outside the range defined by the red line is considered as the starting point of the transient mode.

To facilitate a comparison between different conditions, the time of the last data point in the periodic steady-state condition is set to zero for all cases. Figure 3.7 displays the decay of the

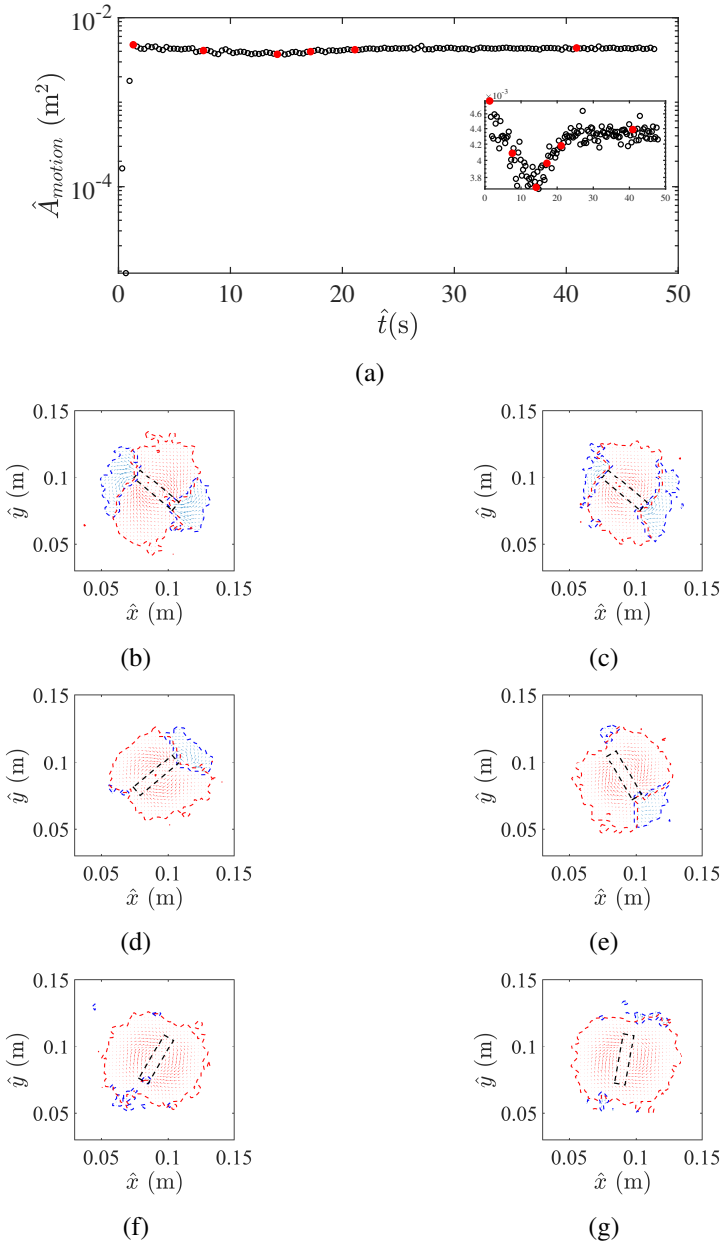

Figure 3.3: Illustration of (a) evolution of systematically flowing area ($\hat{A}_{motion}$) at angular velocity of 400 rpm and rod length of 3.8 cm (b,c,d,e,f,g) snapshots of the velocity field. The red markers in 3.3a indicate times when the snapshots are taken. Red vectors indicate fluid movement in a clockwise direction, enclosed by corresponding red dashed lines. Similarly, blue vectors depict fluid motion in a counterclockwise direction, enclosed by corresponding blue dashed lines. The dashed black line shows the position of the rod. The fluid properties are: $\hat{\tau_y} = 0.33$ Pa, $\hat{K} = 0.66$ Pa.s^n, and $n = 0.44$.

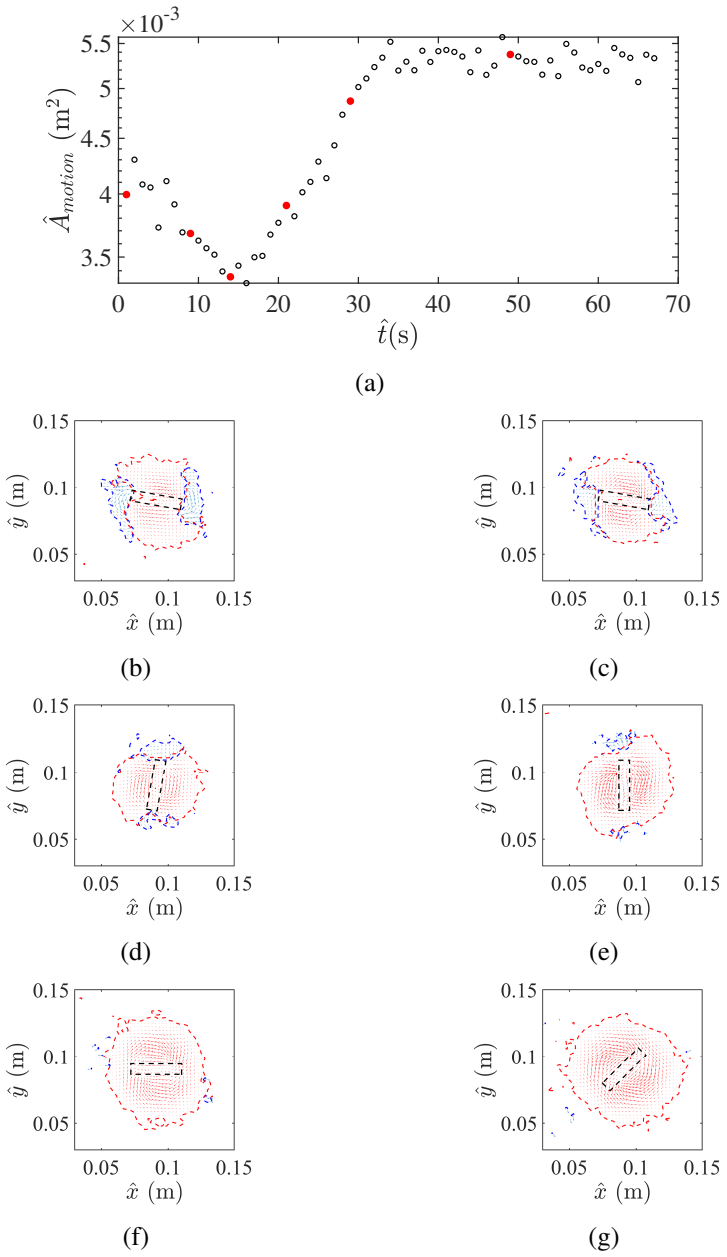

Figure 3.4: Illustration of (a) evolution of systematically flowing area ($\hat{A}_{motion}$) at angular velocity of 500 rpm and rod length of 3.8 cm (b,c,d,e,f,g) snapshots of the velocity field. The red markers in 3.4a indicate times when the snapshots are taken. Red vectors indicate fluid movement in a clockwise direction, enclosed by corresponding red dashed lines. Similarly, blue vectors depict fluid motion in a counterclockwise direction, enclosed by corresponding blue dashed lines. The dashed black line shows the position of the rod. The fluid properties are: $\hat{\tau_y} = 0.33$ Pa, $\hat{K} = 0.66$ Pa.s^n, and $n = 0.44$.

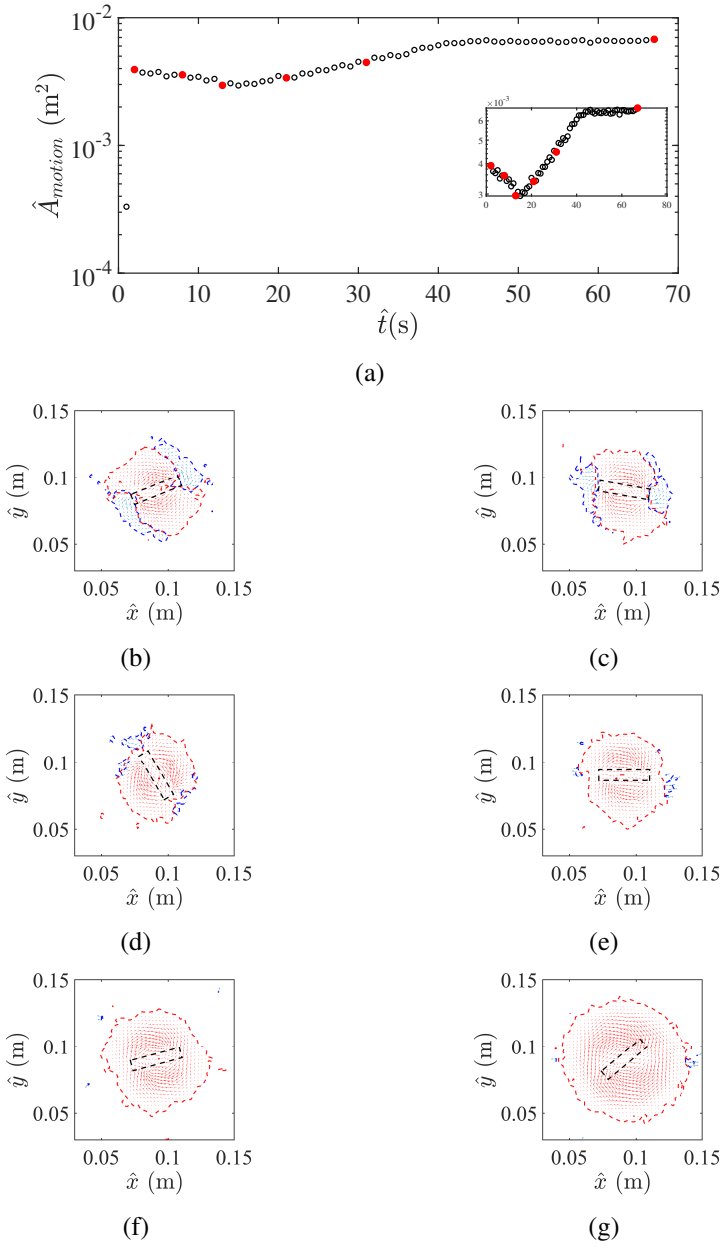

Figure 3.5: Illustration of (a) evolution of systematically flowing area ($\hat{A}_{motion}$) at angular velocity of 600 rpm and rod length of 3.8 cm (b,c,d,e,f,g) snapshots of the velocity field. The red markers in 3.5a indicate times when the snapshots are taken. Red vectors indicate fluid movement in a clockwise direction, enclosed by corresponding red dashed lines. Similarly, blue vectors depict fluid motion in a counterclockwise direction, enclosed by corresponding blue dashed lines. The dashed black line shows the position of the rod. The fluid properties are: $\hat{\tau_y} = 0.33$ Pa, $\hat{K} = 0.66$ Pa.s^n, and $n = 0.44$.

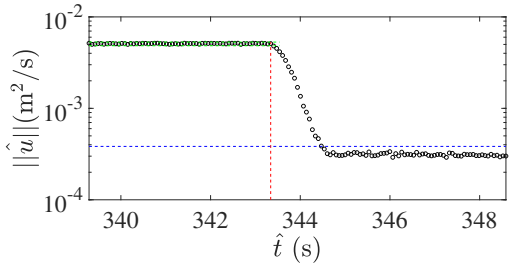

Figure 3.6: The velocity norm versus time for rod length of 3.8 cm and angular velocity of 300 rpm. The dashed green lines represent the upper and lower bounds of the steady velocity norm. The dashed red line shows the starting point of transient mode. The dashed blue line marks the distinction between the systematic movement and the stationary state.

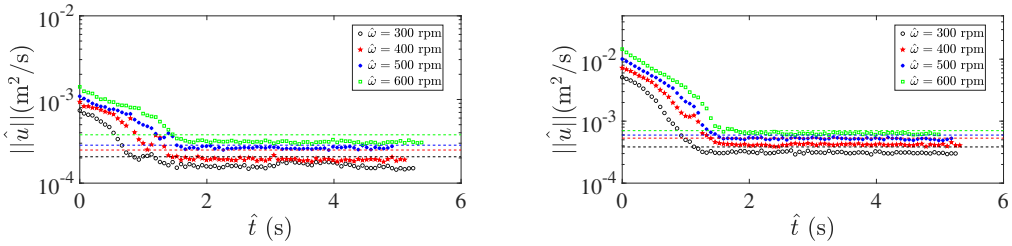

(a) (b)

Figure 3.7: The decay of velocity norm at different angular velocities and rod length of (a) 1.9 cm; (b) 3.8 cm. The dashed colorful lines mark the distinction between the systematic movement and the stationary state. The fluid properties are: $\hat{\tau_y} = 0.33$ Pa, $\hat{K} = 0.66$ Pa.s$^{\mathrm{n}}$, and $n = 0.44$.

velocity norm at different rod lengths and angular velocities. In both cases, the velocity norm decreases over time, indicating a decay of the flow. Figure 3.8 indicates the time that takes the flow to become motionless (decay time, $\hat{t}_{||\hat{u}||,decay}$) which is extracted from figure 3.7. The decay time increases by increasing the angular velocities. However, it is observed that at higher angular velocities, the rate of change in the decay time decreases. This suggests that the effect of angular velocity on the decay time becomes less significant as the angular velocity reaches higher values.

3.3 Cavern shape

In this study, we examined the characteristics of the cavern using both the velocity field (based on PIV measurements) and the intensity field (Dye Visualization).

In the case of the velocity field analysis, we explored two different criteria for defining the

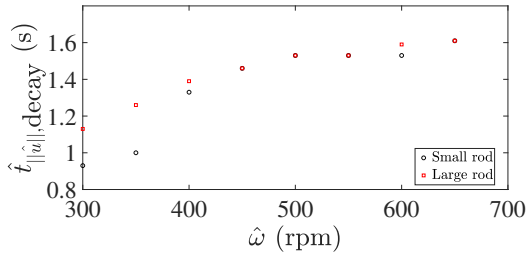

Figure 3.8: Velocity norm stoppage time (the time needed steady velocity norm to reach motionless state after turning the rod off) versus angular velocities at different rod lengths. The fluid properties are: $\hat{\tau_y} = 0.33$ Pa, $\hat{K} = 0.66$ Pa.s$^{\text{n}}$, and $n = 0.44$.

boundaries of the cavern. First, the cavern is defined as the area where the magnitude of the velocity exceeds two percent of the maximum velocity at the tip of the rod. The area of the cavern characterized using this criterion is denoted by $\hat{A}_{CP}$. The second criterion defines the cavern boundary as separating the regions with systematically flowing from those with stagnant fluid. This area is denoted by $\hat{A}motion$.

For the intensity field analysis, the area of the cavern ($\hat{A}_{CD}$) was determined using image analysis. This algorithm involves setting a specific threshold value for pixel intensity to distinguish areas in the tank without dye. Pixels with intensity values above the threshold are considered part of the dye-filled region and are used to measure the cavern's size. Prior to dye injection, an image is captured, and the intensity field is computed. The average intensity value is then regarded as the threshold, and any region with intensity values lower than this threshold is identified as the area filled with dye.

Figures 3.9 and 3.10 illustrate the cavern shape ($\hat{A}_{CP}$) at different values of Re and AR. By examining both figures, it can be observed that when inertial forces dominate, the shape of the cavern becomes less dependent on the position of the rod. At lower Re values (for both ratios of rod diameter to thickness), the location of well-mixed zones changes with variations in the rod position.

Figure 3.11 illustrates the dependency of the cavern boundary ($\hat{A}_{CP}$) on the position of the rod at lower values of Re. It is observed that by changing the phase angle of the rod, the boundaries of the cavern also change. This finding confirms that using the velocity criterion to define the cavern boundaries at a specific angle of the rod is unable to accurately predict the size of the cavern

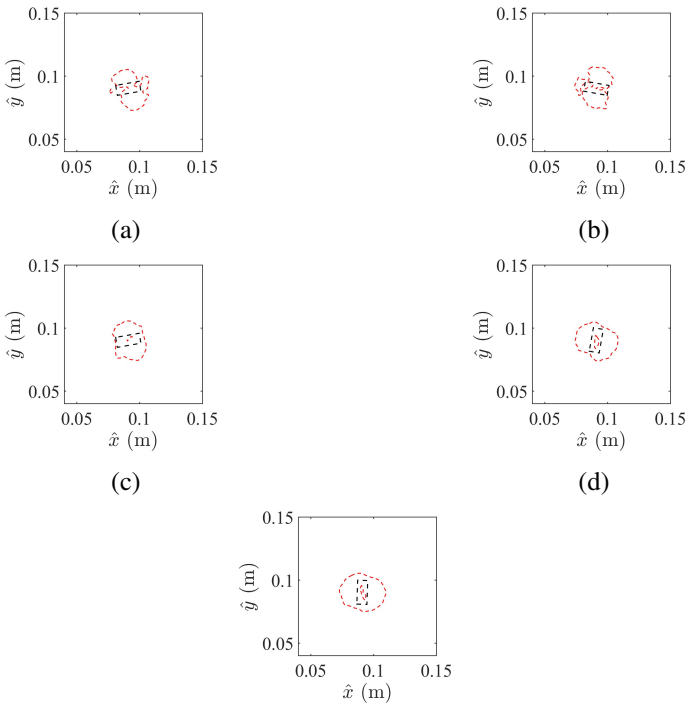

Figure 3.9: Cavern shapes ($\hat{A}_{CP}$) at AR=2.4 and at (a) Re=123; (b) Re=194; (c) Re=278; (d) Re=371; (e) Re=422. The dashed red lines represent the cavern boundary. The dashed black line shows the position of the rod.

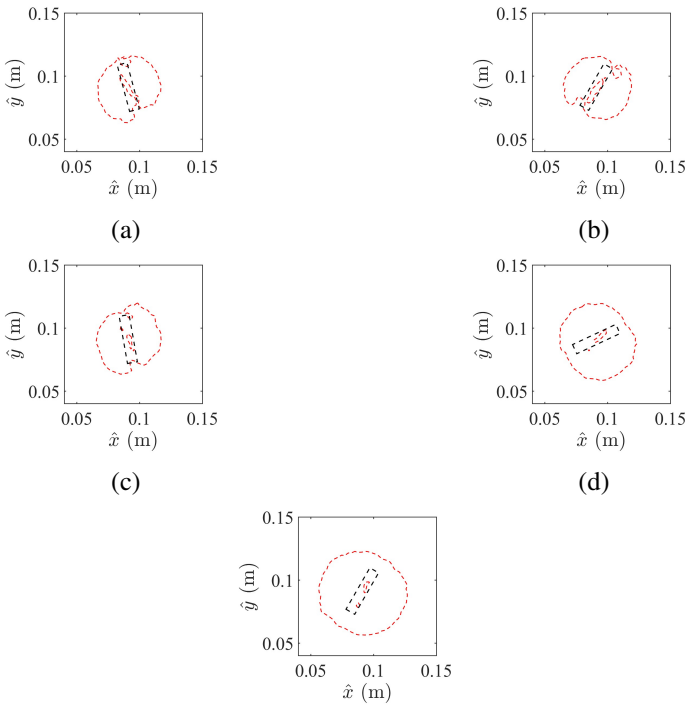

Figure 3.10: Cavern shapes ($\hat{A}_{CP}$) at AR=4.8 and at (a) Re=89; (b) Re=140; (c) Re=321; (d) Re=549; (e) Re=820. The dashed red lines represent the cavern boundary. The dashed black line shows the position of the rod.

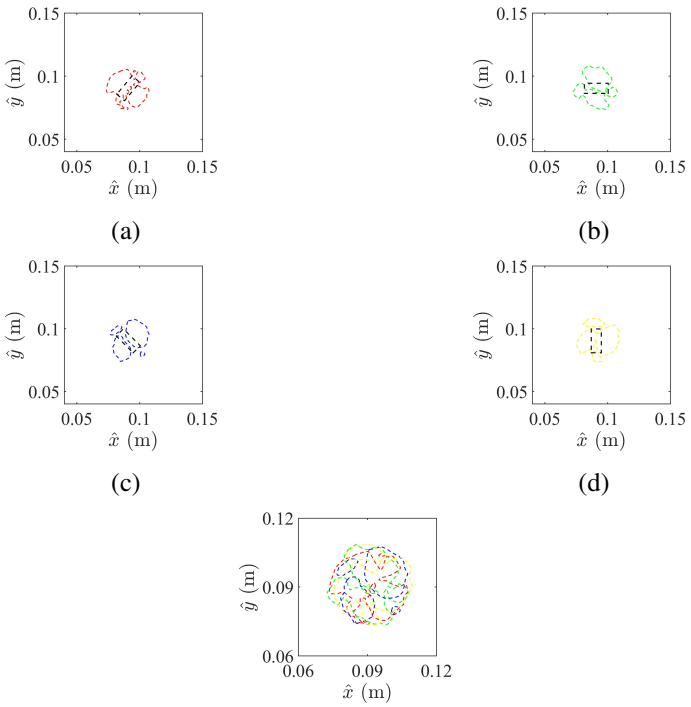

Figure 3.11: (a,b,c,d) Cavern shapes ($\hat{A}_{CP}$) at different rod positions, Re=123, and AR=2.4. (e) Overlaying cavern boundaries shown in 3.11a, 3.11b, 3.11c, and 3.11d. The dashed red, green, blue, and yellow lines represent the cavern boundaries. The dashed black line shows the position of the rod.

when viscous forces dominate. In such cases, it is necessary to overlay the cavern boundaries obtained at different positions of the rod (as shown in figures 3.11e). By plotting these boundaries together, the shape of the cavern appears to be circular (figure 3.11e), indicating a more accurate representation of the cavern shape. This indicates that while the cavern area reaches a steady-state level, the cavern shape does not stabilize, and its boundary undergoes changes due to the rotation of the rod. However, figure 3.12 demonstrates that at higher values of Re, the dependency of cavern boundaries on the rod position decreases. In this case, determining the cavern based on the velocity criterion can more accurately predict the size of the cavern, regardless of the phase angle of the rod. This finding suggests that when inertial forces are dominant, the velocity criterion becomes a more reliable method for determining cavern boundaries, and the impact of the rod position on cavern size diminishes.

Figures 3.13 and 3.14 illustrate the systematically flowing area ($\hat{A}_{motion}$) at different values of

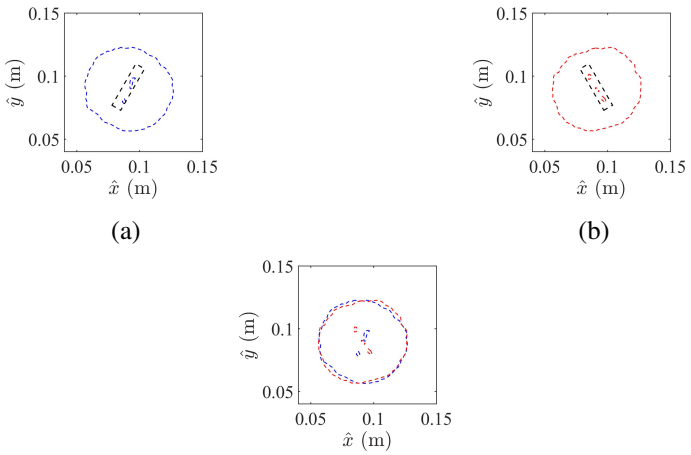

Figure 3.12: (a,b) Cavern shapes ($\hat{A}_{CP}$) at different rod positions, Re=820, and AR=4.8. (c) Overlaying cavern boundaries shown in 3.12a and 3.12b. The dashed red and blue lines represent the cavern boundaries. The dashed black line shows the position of the rod.

Reynolds number (Re) and aspect ratio (AR). Similar to the behavior observed for $\hat{A}_{CP}$, as the Reynolds number increases, the influence of the rod position on the shape of the systematically flowing area diminishes.

Another approach to characterize the current flow problem is using Dye Visualization technique. Images are captured under various operating conditions and viewpoints, including side and top views. The side view images capture the cavern height, while the top view images depict the cavern area in the horizontal plane (figure 3.15). In figure 3.16, the cavern shape is illustrated at different values of Re. Interestingly, the shape of the cavern appears to be almost independent of the rod position, even when viscous forces dominate. This is in contrast to the results obtained using the velocity criterion, where the cavern shape was highly dependent on the rod position at lower Re values. These findings suggest that the cavern shape obtained through the velocity criterion may not necessarily be similar to those obtained using the intensity criterion. However, when inertial forces are dominant, the cavern shape exhibits similarities regardless of the criterion used (velocity or intensity threshold).

Exploring the cavern shape through the application of two distinct criteria ($\hat{A}_{CP}$ and $\hat{A}_{motion}$) for defining cavern boundaries reveals the positional influence of the rod at lower Reynolds numbers. However, this influence is not evident when cavern is characterized based on the intensity field. To

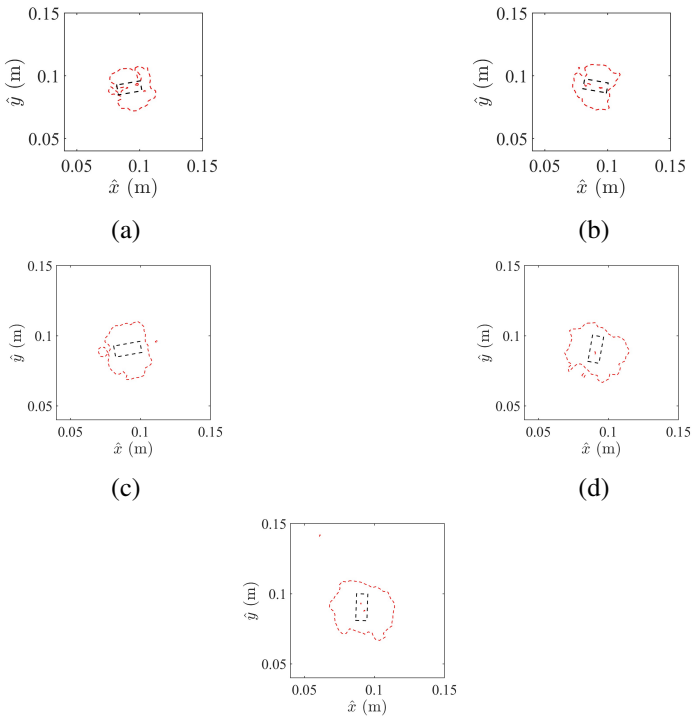

Figure 3.13: Systematically flowing area ($\hat{A}_{motion}$) at AR=2.4 and at (a) Re=123; (b) Re=194; (c) Re=278; (d) Re=371; (e) Re=422. The dashed red lines represent the boundary. The dashed black line shows the position of the rod.

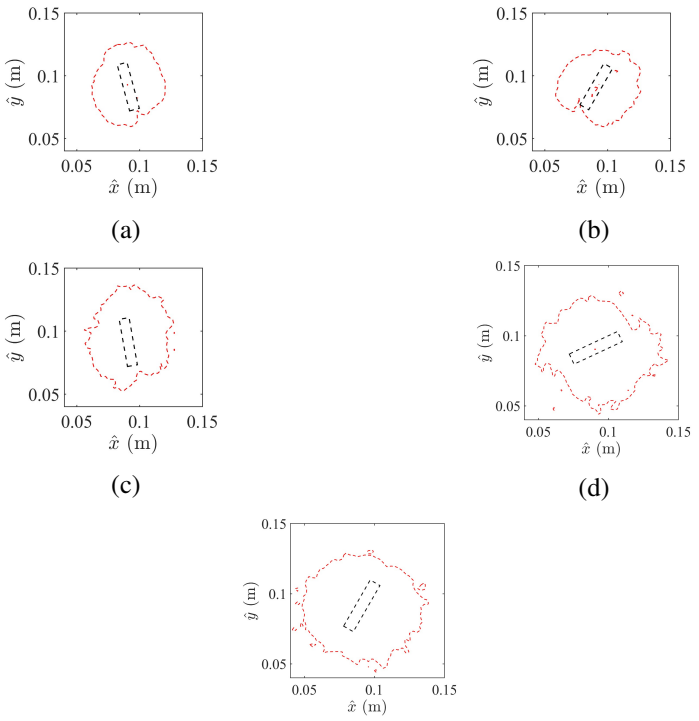

Figure 3.14: Systematically flowing area ($\hat{A}_{motion}$) at AR=4.8 and at (a) Re=89; (b) Re=140; (c) Re=321; (d) Re=549; (e) Re=820. The dashed red lines represent the boundary. The dashed black line shows the position of the rod.

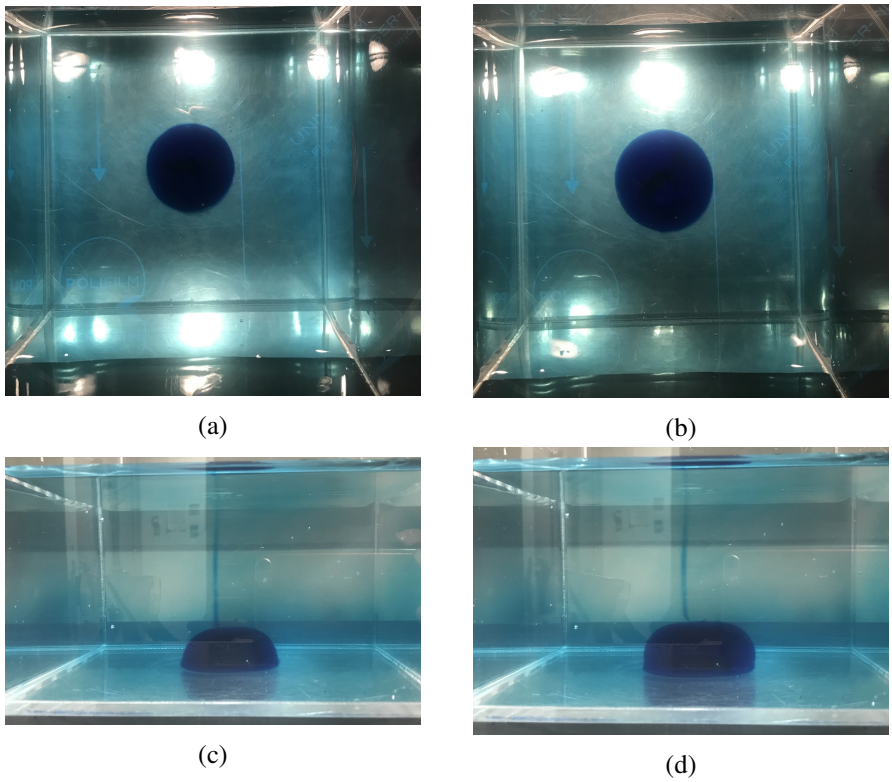

(a) (b) (c) (d)

Figure 3.15: Illustration of cavern (colorful shapes) (a,b) top view; (c,d) side view.

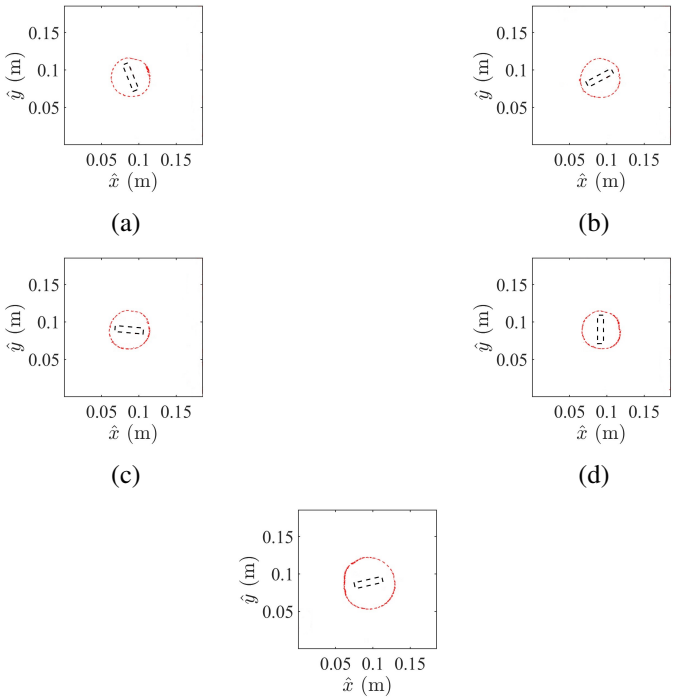

Figure 3.16: Cavern shapes ($\hat{A}_{CD}$) at AR=4.8 and (a) Re=123; (b) Re=194; (c) Re=321; (d) Re=549; (e) Re=820. The dashed red line represents the cavern boundary. The dashed black line shows the position of the rod.

facilitate a comparison between cavern shapes established via velocity and intensity criteria, the superimposition of caverns obtained from the velocity field, particularly at lower Reynolds numbers, becomes essential to mitigate the rod's positional impact on cavern boundaries.

3.4 Cavern area and height

The dimensionless representations of cavern area (obtained both from velocity and intensity fields) and cavern height are listed below.

$$A_{CP} = \frac{\hat{A}_{CP}}{\hat{D}^2} \tag{23}$$

$$A_{CD} = \frac{\hat{A}_{CD}}{\hat{D}^2} \tag{24}$$

$$h = \frac{\hat{h}}{\hat{D}} \tag{25}$$

A_{CP} and A_{CD} quantify the cavern area. h expresses the ratio of cavern height (obtained through the Dye Visualization technique) to rod diameter.

Figure 3.17 displays the relationship between A_{CP} and Re for different AR. As Re increases, the dimensionless cavern area increases. This growth occurs in two distinct stages. In the first stage (e.g., $Re < 300$ in figure 3.17a), the rate of cavern size growth is relatively slow. However, during the second stage, this growth rate accelerates. This behavior is observed for both values of AR. It indicates that when inertial forces become dominant, the rate of cavern size expansion significantly increases.

Figure 3.18 displays the dimensionless representation of cavern area, A_{CP}(overlaid), achieved by superimposing caverns at varying rod positions. This approach yields a circular cavern shape (figure 3.11e), aligning with the forms derived from intensity field analysis. The enclosed region within caverns at different rod positions is quantified for various Reynolds numbers and aspect ratios.

Figure 3.19 represents the dimensionless cavern area (A_{CP}) for different fluid concentrations.

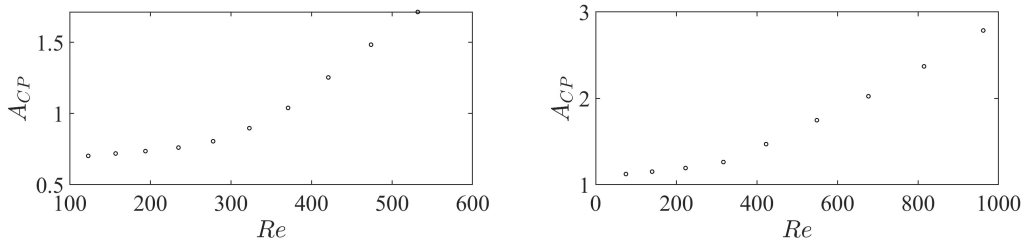

(a) (b)

Figure 3.17: The steady-state dimensionless form of cavern area (A_{CP}) at different Re values and (a) AR=2.4; (b) AR=4.8.

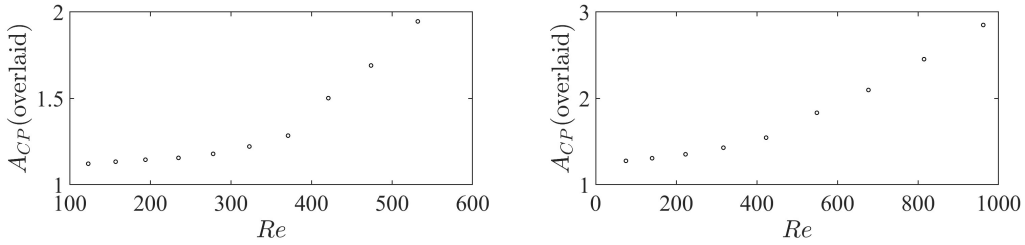

(a) (b)

Figure 3.18: The steady-state dimensionless form of overlaid cavern area at different Re values and (a) AR=2.4; (b) AR=4.8.

The depicted red line corresponds to a first-order exponential curve fit applied to the data. The curve-fit equation is expressed as follows:

$$A_{CP} = a \cdot \exp(b \cdot Re) \tag{26}$$

where the constants are $a = 0.9276$ and $b = 0.0011$.

Figure 3.20 displays the dimensionless cavern area (A_{CD}) as a function of Re. Similar to the cavern area obtained using the velocity criterion, there is an initial slower increase followed by a faster growth rate. Figure 3.21 presents the cavern height, which is obtained from the side-view images, at different Re values. It can be observed that the cavern height increases as the Re values increase. This behavior can be attributed to the increasing strength of the inertial term as Re rises. The heightened influence of inertial forces leads to an increase in the cavern height. Furthermore, the growth rate of the cavern height accelerates at higher Re values.

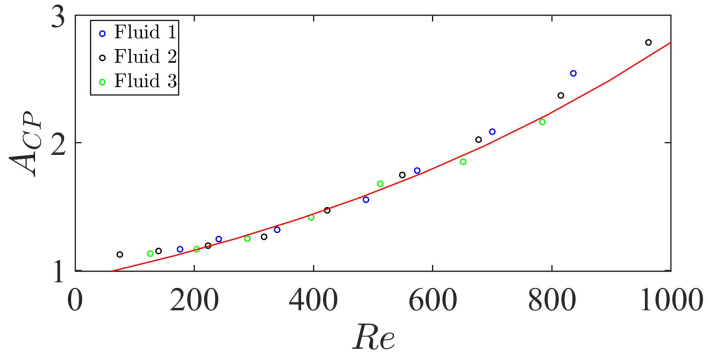

Figure 3.19: The steady-state dimensionless form of cavern area (A_{CP}) at different Re values and fluid cases (AR=4.8). The red line corresponds to a first-order exponential curve fit applied to the data.

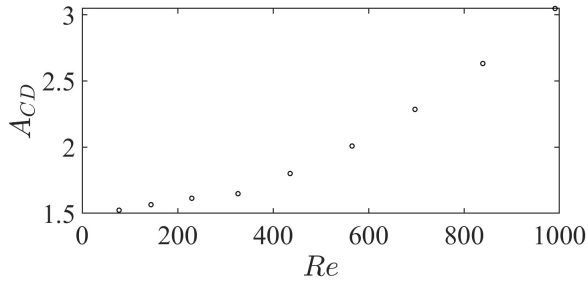

Figure 3.20: The steady-state dimensionless form of cavern area (A_{CD}) at different Re values and AR=4.8.

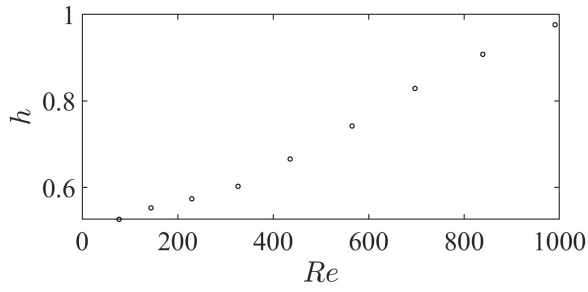

Figure 3.21: The steady-state dimensionless form of cavern height at different Re values and AR=4.8.

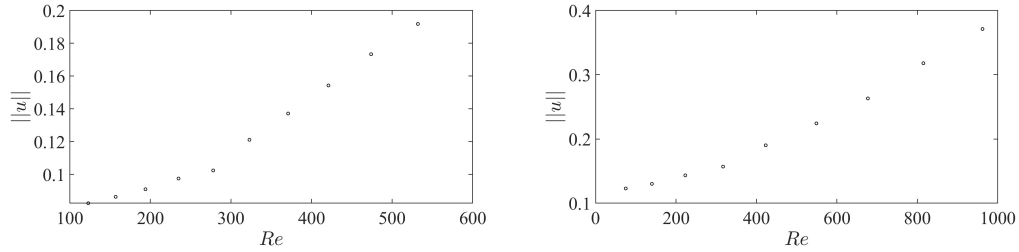

(a) (b)

Figure 3.22: The steady-state dimensionless form of velocity norm at different Re values and (a) AR=2.4; (b) AR=4.8.

3.5 Velocity norm

In this section, the velocity norm is measured upon achieving a state of steady-state condition, where the recorded values remain relatively constant over time without significant fluctuations. The dimensionless representation of velocity norm is listed below.

$$||u|| = \frac{||\hat{u}||}{\hat{\Omega}\hat{D}^2} \tag{27}$$

$||u||$ represents the velocity norm in the measurement plane, which serves as an indicator of the kinetic energy of the fluid. Figure 3.22 presents the dimensionless velocity norm. Similar to the cavern area, the velocity norm demonstrates an increase as the ratio of inertial to viscous forces rises, but in two distinct phases. In both cases of AR values, the growth rate during the first phase is slower compared to the second phase.

Chapter 4

Conclusion and future work

4.1 Conclusion

The mixing characteristics of Carbopol solutions in a magnetic mixer were investigated experimentally. Different Carbopol solutions were prepared with concentrations of 0.35, 0.4, and 0.45 grams per liter. To assess the rheological properties of Carbopol gels, a hybrid DHR20 TA rheometer was employed. Rheology tests were conducted using the stress-strain ramp method to determine the yield stress. The experiment utilized a transparent acrylic rectangular tank with a square cross-section measuring 20 cm in length. Two rods, both with the same thickness, were used in this research, one with a length of 1.9 cm and the other with a length of 3.8 cm.

PIV analysis was used to obtain the velocity field. Also, Dye Visualization technique helped to characterize cavern. Measurements and analysis were performed on the velocity norm and cavern size. A dimensionless number, Re, representing the ratio of inertial to resistant forces (flow stress), was utilized in the study. The study explored the flow development, periodic steady-state, and the flow stoppage behaviors. To characterize the cavern, three distinct definitions were introduced, A_{CP}, A_{CD}, and A_{motion}.The key findings from the research are summarized as follows:

- The development pattern of the instantaneous angular velocity and the velocity norm displays a similar trend. This indicates that the evolution path the fluid undergoes is not attributed to the shear thinning behavior of the fluid. As the yield stress and consistency increase, there is a corresponding decrease in the velocity norm.

- When the solution was motionless, the velocity field was captured. By analyzing the velocity field, a velocity threshold was introduced, above which an area was defined as systematically flowing region. The findings indicated that the area of systematically flowing initially decreases, followed by an increase until it stabilizes at a steady-state condition. This observed behavior can be ascribed to the evolution of velocity field vectors.

- Decay of the kinetic energy was investigated by collecting data after the stirrer is turned off. Decay time was defined as the time that takes the flow to become motionless. The findings from the flow stoppage experiments indicated that as the angular velocities increase, the decay time also increases. However, it's noticeable that at higher angular velocities, the rate at which the decay time changes becomes slower. This implies that the impact of angular velocity on the decay time diminishes as the angular velocity reaches higher levels.

- Our experiments revealed that the velocity norm and cavern area (A_{CP}) increased with Re. Initially, at lower values of Re where viscous forces were dominant, the growth rate of the flow parameters was relatively slow. However, as Re increased to higher values, the velocity norm and cavern area increased rapidly.

- Another observation pertained to the shape of the cavern. While the area of the cavern (A_{CP}) reached a steady state after a certain amount of time, the shape of the cavern exhibited time-dependent characteristics, particularly at lower Re values. In cases where viscous forces were dominant, the shape of the cavern was influenced by the position of the rod. However, as Re increased, this dependency diminished and the cavern shape approached a more stable form. Therefore, to achieve a more accurate estimation of the size and shape of the cavern at lower Reynolds numbers, we recommend that the cavern boundaries at different phase angles of the rod are overlaid to create a superimposed representation. The area surrounded by the superimposed shape provides a more accurate estimate of the cavern.

- Dye Visualization technique was employed to analyze and compare the characteristics of the cavern with the results obtained from PIV. The investigation focused on examining the behavior of cavern area (A_{CD}) and height as Re was increased. Moreover, a comparison was

made between the cavern shapes obtained through both techniques. The results from the Dye Visualization technique indicated that cavern shapes reached a steady form regardless of the value of Re and were not influenced by the position of the rod. This finding aligned with the cavern shapes (A_{CP}) observed through PIV when Re reached higher values.

4.2 Future work

There are several avenues for further exploration and research that can expand upon the findings presented here. The following areas are suggested for future work:

- Investigating the mixing time and understanding how it behaves when inertial forces start to dominate is a crucial aspect of the next studies. By delving into the analysis of mixing time under different Reynolds numbers, novel insights and observations are uncovered that can significantly contribute to our understanding of fluid dynamics and mixing processes.

- Power consumption is an additional mixing characteristic that can be quantified both in transient and steady-state conditions. The intriguing prospect lies in monitoring power consumption from the moment the impeller initiates its rotation until the fluid attains a steady-state level, and examining its behavior throughout this process.

- Determining the cavern area by measuring the concentration field, possibly utilizing techniques such as Planar Laser-Induced Fluorescence. This approach would entail capturing data at a specific plane and subsequently comparing the results with those obtained through PIV analysis.

Appendix A

A.1 Rheometry

The behavior of yield stress is commonly characterized by measuring the variation of the steady shear stress with the strain rate. However, different studies have shown that precise measurement of the fluids rheological properties is quite challenging (Coussot, 2005; Ovarlez & Hormozi, 2019). One of the most important goals of rheometry is to simplify the problem to study the behavior of complex fluids. In rheometry, we often consider flow configurations where all components of strain rate tensor are zero except one; i.e. most flows considered are simple shear flows. This simplification is sufficient to investigate the flow behavior in various situations, such as pipe flows. Figure A.1 shows a schematic representation of a simple shear. In rheology tests, the simple shear flow is achieved by three major configurations, cone and plate, parallel plates, and Couette (Figure A.2).

When investigating the flow characteristics of yield stress fluids, slip at the wall may have a considerable effect on the flow behavior. The material behavior changes when slip occurs because

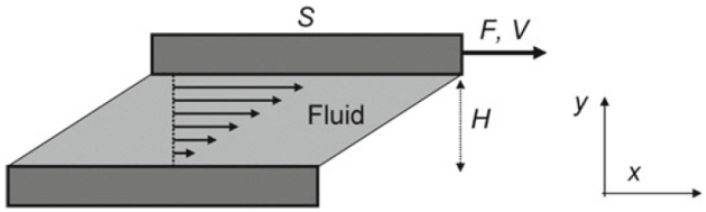

Figure A.1: Schematic representation of a simple shear experiment (Ovarlez & Hormozi, 2019)

the material will flow by applying the stress value of less than the yield stress. This problem can be avoided by using rough or treated wall surfaces.

A.1.1 Viscometric flows

Cone and plate

In the cone and plate configuration, the fluid is placed between a cone and a plate with identical symmetry axis and radius. Simple shear is created when the cone rotates around the symmetry axis with a constant angular velocity and the plate is fixed.

To have a homogeneous stress distribution, the cone angle should be small. For example, when the cone angle is 4°, shear stress difference from the plate to the cone is about 0.5% (Coussot, 2005). The spherical coordinates connected to the plate (r, θ, φ) are considered for this geometry and the cone angular velocity is Ω. The flow is symmetric with respect to the cone axis and the velocity and stress tensor are not dependent on φ. The only nonzero velocity component is v_φ. This velocity component can be defined as:

$$v_\varphi = r\omega \tag{28}$$

ω is a function of θ. By assuming the uniform and homogeneous stress in the gap, the shear rate would be constant. Hence, if the cone angle is small enough to be able to reach homogeneous simple shear and the no-slip condition is valid for both surfaces, shear rate, $\dot{\gamma}$, is obtained from this simple equation:

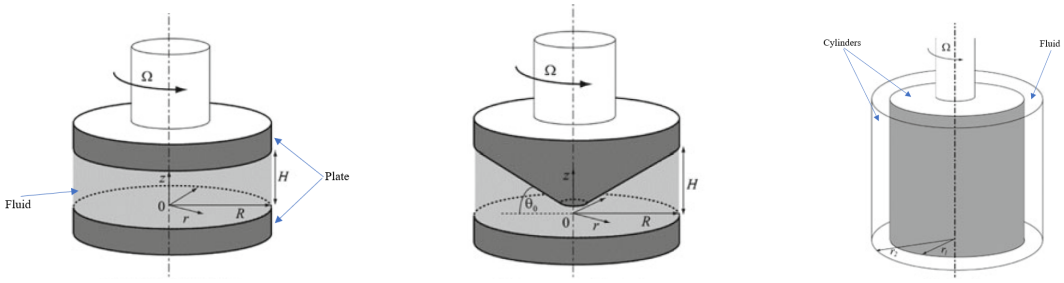

(a) Parallel plate (b) Cone and plate (c) Couette

Figure A.2: Three main standard geometries (Ovarlez & Hormozi, 2019)

$$\dot{\gamma} = \frac{\Omega}{\theta_0} \tag{29}$$

where Ω and θ_0 are the cone angular velocity and cone angle. Also, shear stress can be obtained from equation (30).

$$\tau = \frac{3T}{2\pi R^3} \tag{30}$$

where T is the torque resulting from the shear stress on the cone surface.

Parallel plates

In this geometry, the material is placed between two parallel discs. Two discs have the same symmetry axis and radius and they are separated by a gap with a height of H. To impose shear, the upper plate rotates around the central axis with a constant velocity, Ω, and the bottom plate is fixed. As it is shown in figure A.2, the cylindrical coordinates (r, θ, z) are connected to the bottom plate. Because of the symmetric flow, velocity does not change with θ and the only nonzero velocity component is the tangential one, $\upsilon_\theta = \upsilon_\theta(r, z)$. Velocity at the fixed bottom plate is $\upsilon_\theta(r, 0) = 0$ and at the upper plate is $\upsilon_\theta(r, z_0) = \Omega r$. The velocity field that can satisfy the boundary conditions is defined as $\upsilon_\theta(r, z) = \frac{\Omega r z}{H}$. Also, the shear rate is obtained:

$$\dot{\gamma} = \frac{\Omega r}{H} \tag{31}$$

Because the shear rate is not homogeneous (it is a function of r) in the gap, the shear stress is also a function of radius:

$$\tau(r) = \frac{1}{2\pi r^2}\frac{dT}{dr} \tag{32}$$

Couette geometry

In this geometry, there are two coaxial cylinders with certain inner (R_i) and outer radii (R_o). The material is placed in the gap between them and the shear is imposed by rotating the inner cylinder

(with a hight of H) at a constant velocity, Ω. The outer cylinder is fixed. In addition, the radial gap between the cylinders is much smaller than the gap between the inner cylinder and the bottom of the cup. Velocity doesn't change with θ and z and the tangential velocity is the only nonzero velocity in the gap. The shear stress can be defined as:

$$\tau(r) = \frac{T}{2\pi H r^2} \tag{33}$$

When the gap between cylinders is small ($R_o - R_i < 0.005 \times R_i$) (Ovarlez & Hormozi, 2019), shear stress can be assumed homogeneous and constant in the whole gap. By considering the no-slip condition, shear rate and shear stress are:

$$\dot{\gamma} = \frac{\Omega R_i}{R_o - R_i} \tag{34}$$

$$\tau = \frac{T}{2\pi H R_i^2} \tag{35}$$

However, when the wide gap is used, the distribution of shear stress is highly inhomogeneous. Using wide gap geometry is useful when the flow behavior of suspensions with large particles is characterized.

A.1.2 Rheometry tests

As it is discussed, a yield stress fluid will flow if the value of shear stress is larger than the yield stress. Hence, rheometrical methods should be used to distinguish between solid and liquid regimes. There are two main methods (Ovarlez & Hormozi, 2019) to measure the flow curve $\tau = f(\dot{\gamma})$: creep and ramp tests.

Creep test

In this method, a series of constant shear stresses τ_i over a long period of time are applied. When the value of applied shear stress is greater than the yield stress, the shear rate changes with time and approaches a steady non-zero value. On the contrary, if the applied shear stress is less than

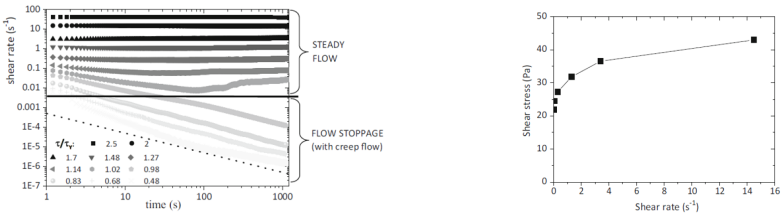

(a) (b)

Figure A.3: (a) Shear rate versus time for different rate of shear stress to yield stress; (b) Steady state shear stress versus shear rate. Adapted from Balmforth et al. (Balmforth et al., 2014)

the yield stress, shear rate will decrease as the steady state is approached. Figure A.3a shows an illustrative case. After applying different values of shear stresses and measuring the corresponding steady values of shear rates, the steady-state data can be used to determine the flow curve (see figure A.3b).

Ramp test

Ramp tests can be used to draw the flow curve faster than creep test (Ovarlez & Hormozi, 2019). When a simple yield stress fluid is investigated, the flow history has no effect on the fluid behavior (Coussot, 2005). This means that by changing the shear rate or shear stress, the fluid reaches its new steady condition within a second (Ovarlez & Hormozi, 2019). Also, according to the result of Balmforth et al. (2014), the shear rate does not change with time when the applied shear stress is larger than the yield stress. In ramp tests, the value of shear stresses or shear rates is continuously increasing (or decreasing) and the corresponding value of shear rates or shear stresses is recorded. In order to check the steady state behavior of the simple yield stress fluid, the behavior of the fluid is also investigated when it turns from a liquid state to a solid state. Hence, an up-ramp is usually followed by a down-ramp (Figure A.4). When analyzing the data, it may be noted that there are some discrepancies between up-ramp and down-ramp results. One way to avoid these discrepancies is to change the value of shear stresses (or shear rates) with a slower rate (Ovarlez & Hormozi, 2019).

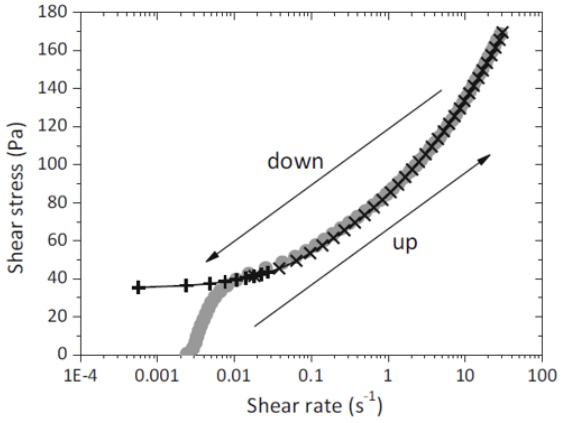

Figure A.4: Shear stress against shear rate for increasing and decreasing stress values (Ovarlez & Hormozi, 2019)

Nomenclature

$\hat{\dot{\gamma}}$	Strain rate
$\hat{\eta}$	Apparent viscosity
$\hat{\mu}_p$	Plastic viscosity
$\hat{\Omega}$	Angular velocity
$\hat{\rho}$	Density
$\hat{\tau}$	Stress tensor
$\hat{\tau}_y$	Yield stress
$\hat{A}_{CD}$	Area characterized by Dye Visualization
$\hat{A}_{CP}$	Area characterized by PIV
$\hat{A}_{motion}$	Systematically flowing area
$\hat{b}$	Rod's tickness
$\hat{D}$	Rod's diameter
$\hat{K}$	Consistency
$\hat{t}_{cc}$	cross-correlation time
$\hat{u}$	x-component of velocity
$\hat{V}$	Velocity magnitude

$\hat{v}$	y-component of velocity
AR	Aspect ratio
Bn	Bingham number
n	Power-law index
Re	Reynolds number

References

Adams, L., & Barigou, M. (2007). Cfd analysis of caverns and pseudo-caverns developed during mixing of non-newtonian fluids. *Chemical Engineering Research and Design*, *85*(5), 598–604.

Adrian, R. J., & Westerweel, J. (2011). *Particle image velocimetry* (No. 30). Cambridge university press.

Amanullah, A., Hjorth, S., & Nienow, A. (1997). Cavern sizes generated in highly shear thinning viscous fluids by scaba 3shp1 impellers. *Food and Bioproducts Processing*, *75*(4), 232–238.

Amanullah, A., Hjorth, S., & Nienow, A. (1998). A new mathematical model to predict cavern diameters in highly shear thinning, power law liquids using axial flow impellers. *Chemical Engineering Science*, *53*(3), 455–469.

Amanullah, A., Serrano-Carreon, L., Castro, B., Galindo, E., & Nienow, A. (1998). The influence of impeller type in pilot scale xanthan fermentations. *Biotechnology and bioengineering*, *57*(1), 95–108.

Ameur, H. (2016a). 3d hydrodynamics involving multiple eccentric impellers in unbaffled cylindrical tank. *Chinese Journal of Chemical Engineering*, *24*(5), 572–580.

Ameur, H. (2016b). Agitation of yield stress fluids in different vessel shapes. *Engineering Science and Technology, an International Journal*, *19*(1), 189–196.

Ameur, H. (2020). Newly modified curved-bladed impellers for process intensification: Energy saving in the agitation of hershel-bulkley fluids. *Chemical Engineering and Processing-Process Intensification*, *154*, 108009.

Ameur, H., Bouzit, M., & Ghenaim, A. (2015). Numerical study of the performance of multistage

scaba 6srgt impellers for the agitation of yield stress fluids in cylindrical tanks. *Journal of Hydrodynamics, Ser. B*, *27*(3), 436–442.

Ameur, H., & Vial, C. (2020). Modified scaba 6srgt impellers for process intensification: Cavern size and energy saving when stirring viscoplastic fluids. *Chemical Engineering and Processing-Process Intensification*, *148*, 107795.

Aref, H., Blake, J. R., Budišić, M., Cardoso, S. S., Cartwright, J. H., Clercx, H. J., ... others (2017). Frontiers of chaotic advection. *Reviews of Modern Physics*, *89*(2), 025007.

Arratia, P., Kukura, J., Lacombe, J., & Muzzio, F. (2006). Mixing of shear-thinning fluids with yield stress in stirred tanks. *AIChE journal*, *52*(7), 2310–2322.

Balmforth, N. J., Frigaard, I. A., & Ovarlez, G. (2014). Yielding to stress: recent developments in viscoplastic fluid mechanics. *Annual Review of Fluid Mechanics*, *46*, 121–146.

Benhanifia, K., Redouane, F., Lakhdar, R., Brahim, M., Al-Farhany, K., Jamshed, W., ... Raizah, Z. (2022). Investigation of mixing viscoplastic fluid with a modified anchor impeller inside a cylindrical stirred vessel using casson–papanastasiou model. *Scientific Reports*, *12*(1), 17534.

Blackwell, B. C., Deetjen, M. E., Gaudio, J. E., & Ewoldt, R. H. (2015). Sticking and splashing in yield-stress fluid drop impacts on coated surfaces. *Physics of Fluids*, *27*(4).

Bowler, A. L., Bakalis, S., & Watson, N. J. (2020). A review of in-line and on-line measurement techniques to monitor industrial mixing processes. *Chemical Engineering Research and Design*, *153*, 463–495.

Bugay, S., Escudié, R., & Liné, A. (2002). Experimental analysis of hydrodynamics in axially agitated tank. *AIChE journal*, *48*(3), 463–475.

Burghelea, T. (2023). Chaotic mixing of yield stress materials. *Science Talks*, *5*, 100107.

Cortada-Garcia, M., Dore, V., Mazzei, L., & Angeli, P. (2017). Experimental and cfd studies of power consumption in the agitation of highly viscous shear thinning fluids. *Chemical Engineering Research and Design*, *119*, 171–182.

Cortada-Garcia, M., Weheliye, W. H., Dore, V., Mazzei, L., & Angeli, P. (2018). Computational fluid dynamic studies of mixers for highly viscous shear thinning fluids and piv validation. *Chemical Engineering Science*, *179*, 133–149.

Coussot, P. (2005). Rheometry of pastes, suspensions, and granular materials: applications in

industry and environment.

Di Giuseppe, E., Corbi, F., Funiciello, F., Massmeyer, A., Santimano, T., Rosenau, M., & Davaille, A. (2015). Characterization of carbopol® hydrogel rheology for experimental tectonics and geodynamics. *Tectonophysics*, *642*, 29–45.

Ein-Mozaffari, F., & Upreti, S. R. (2009). Using ultrasonic doppler velocimetry and cfd modeling to investigate the mixing of non-newtonian fluids possessing yield stress. *Chemical Engineering Research and Design*, *87*(4), 515–523.

Elson, T., Cheesman, D., & Nienow, A. (1986). X-ray studies of cavern sizes and mixing performance with fluids possessing a yield stress. *Chemical Engineering Science*, *41*(10), 2555–2562.

Galindo, E., Argüello, M. A., Velasco, D., Albiter, V., & Martínez, A. (1996). A comparison of cavern development in mixing a yield stress fluid by rushton and intermig impellers. *Chemical Engineering & Technology: Industrial Chemistry-Plant Equipment-Process Engineering-Biotechnology*, *19*(4), 315–323.

Galindo, E., & Nienow, A. W. (1993). Performance of the scaba 6srgt agitator in mixing of simulated xanthan gum broths. *Chemical Engineering & Technology: Industrial Chemistry-Plant Equipment-Process Engineering-Biotechnology*, *16*(2), 102–108.

Galindot, E., & Nienow, A. W. (1992). Mixing of highly viscous simulated xanthan fermentation broths with the lightnin a-315 impeller. *Biotechnology Progress*, *8*(3), 233–239.

Hirata, Y., Nienow, A. W., & Moore, I. P. (1994). Estimation of cavern sizes in a shear-thinning plastic fluid agitated by a rushton turbine based on lda measurements. *Journal of chemical engineering of Japan*, *27*(2), 235–237.

Hui, L. K., Bennington, C. P., & Dumont, G. A. (2009). Cavern formation in pulp suspensions using side-entering axial-flow impellers. *Chemical engineering science*, *64*(3), 509–519.

Ihejirika, I., & Ein-Mozaffari, F. (2007). Using cfd and ultrasonic velocimetry to study the mixing of pseudoplastic fluids with a helical ribbon impeller. *Chemical Engineering & Technology: Industrial Chemistry-Plant Equipment-Process Engineering-Biotechnology*, *30*(5), 606–614.

Irgens, F. (2014). *Rheology and non-newtonian fluids* (Vol. 190). Springer.

Jaworski, Z., Pacek, A., & Nienow, A. (1994). On flow close to cavern boundaries in yield stress

fluids. *Chemical engineering science*, *49*(19), 3321–3324.

Kazemzadeh, A., Ein-Mozaffari, F., Lohi, A., & Pakzad, L. (2016). Effect of the rheological properties on the mixing of herschel-bulkley fluids with coaxial mixers: Applications of tomography, cfd, and response surface methodology. *The Canadian Journal of Chemical Engineering*, *94*(12), 2394–2406.

Kazemzadeh, A., Ein-Mozaffari, F., Lohi, A., & Pakzad, L. (2017). Intensification of mixing of shear-thinning fluids possessing yield stress with the coaxial mixers composed of two different central impellers and an anchor. *Chemical Engineering and Processing: Process Intensification*, *111*, 101–114.

Lubrizol. (2010). Viscosity of carbopol polymers in aqueous systems [computer software manual].

Myers, K., Ward, R., & Bakker, A. (1997). A digital particle image velocimetry investigation of flow field instabilities of axial-flow impellers.

Nirmalkar, N., Chhabra, R., & Poole, R. (2013). Laminar forced convection heat transfer from a heated square cylinder in a bingham plastic fluid. *International Journal of Heat and Mass Transfer*, *56*(1-2), 625–639.

Ovarlez, G., & Hormozi, S. (2019). *Lectures on visco-plastic fluid mechanics*. Springer.

Pakzad, L., Ein-Mozaffari, F., & Chan, P. (2008a). Measuring mixing time in the agitation of non-newtonian fluids through electrical resistance tomography. *Chemical Engineering & Technology: Industrial Chemistry-Plant Equipment-Process Engineering-Biotechnology*, *31*(12), 1838–1845.

Pakzad, L., Ein-Mozaffari, F., & Chan, P. (2008b). Using computational fluid dynamics modeling to study the mixing of pseudoplastic fluids with a scaba 6srgt impeller. *Chemical Engineering and Processing: Process Intensification*, *47*(12), 2218–2227.

Pakzad, L., Ein-Mozaffari, F., & Chan, P. (2008c). Using electrical resistance tomography and computational fluid dynamics modeling to study the formation of cavern in the mixing of pseudoplastic fluids possessing yield stress. *Chemical Engineering Science*, *63*(9), 2508–2522.

Pakzad, L., Ein-Mozaffari, F., Upreti, S. R., & Lohi, A. (2013a). Agitation of herschel–bulkley fluids with the scaba–anchor coaxial mixers. *Chemical Engineering Research and Design*,

91(5), 761–777.

Pakzad, L., Ein-Mozaffari, F., Upreti, S. R., & Lohi, A. (2013b). Experimental and numerical studies on mixing of yield-pseudoplastic fluids with a coaxial mixer. *Chemical Engineering Communications*, *200*(12), 1553–1577.

Pakzad, L., Ein-Mozaffari, F., Upreti, S. R., & Lohi, A. (2013c). A novel and energy-efficient coaxial mixer for agitation of non-newtonian fluids possessing yield stress. *Chemical Engineering Science*, *101*, 642–654.

Patel, D., Ein-Mozaffari, F., & Mehrvar, M. (2012). Improving the dynamic performance of continuous-flow mixing of pseudoplastic fluids possessing yield stress using maxblend impeller. *chemical engineering research and design*, *90*(4), 514–523.

Paul, E. L., Atiemo-Obeng, V. A., & Kresta, S. M. (2004). *Handbook of industrial mixing*. Wiley Online Library.

Prajapati, P., & Ein-Mozaffari, F. (2009). Cfd investigation of the mixing of yield-pseudoplastic fluids with anchor impellers. *Chemical Engineering & Technology: Industrial Chemistry-Plant Equipment-Process Engineering-Biotechnology*, *32*(8), 1211–1218.

Raffel, M., Willert, C. E., Kompenhans, J., et al. (1998). *Particle image velocimetry: a practical guide* (Vol. 2). Springer.

Raffel, M., Willert, C. E., Scarano, F., Kähler, C. J., Wereley, S. T., & Kompenhans, J. (2018). *Particle image velocimetry: a practical guide*. Springer.

Reynolds, O. (1883). Xxix. an experimental investigation of the circumstances which determine whether the motion of water shall be direct or sinuous, and of the law of resistance in parallel channels. *Philosophical Transactions of the Royal society of London*(174), 935–982.

Russell, A., Kahouadji, L., Shin, S., Chergui, J., Juric, D., Piccione, P. M., … Markides, C. N. (2020). Assessing the mixing effectiveness of dual-impeller systems in the agitation of viscoplastic fluids.

Russell, A. W., Kahouadji, L., Mirpuri, K., Quarmby, A., Piccione, P. M., Matar, O. K., … Markides, C. N. (2019). Mixing viscoplastic fluids in stirred vessels over multiple scales: A combined experimental and cfd approach. *Chemical Engineering Science*, *208*, 115129.

R. Varges, P., M. Costa, C., S. Fonseca, B., F. Naccache, M., & de Souza Mendes, P. R. (2019). Rheological characterization of carbopol® dispersions in water and in water/glycerol solutions. *Fluids*, *4*(1), 3.

Saeed, S., & Ein-Mozaffari, F. (2008). Using dynamic tests to study the continuous mixing of xanthan gum solutions. *Journal of Chemical Technology & Biotechnology: International Research in Process, Environmental & Clean Technology*, *83*(4), 559–568.

Saeed, S., Ein-Mozaffari, F., & Upreti, S. R. (2007). Using computational fluid dynamics modeling and ultrasonic doppler velocimetry to study pulp suspension mixing. *Industrial & engineering chemistry research*, *46*(7), 2172–2179.

Saeed, S., Ein-Mozaffari, F., & Upreti, S. R. (2008). Using computational fluid dynamics to study the dynamic behavior of the continuous mixing of herschel- bulkley fluids. *Industrial & engineering chemistry research*, *47*(19), 7465–7475.

Saramito, P., & Wachs, A. (2017). Progress in numerical simulation of yield stress fluid flows. *Rheologica Acta*, *56*, 211–230.

Savreux, F., Jay, P., & Magnin, A. (2007). Viscoplastic fluid mixing in a rotating tank. *Chemical engineering science*, *62*(8), 2290–2301.

Solomon, J., Elson, T., Nienow, A., & Pace, G. (1981). Cavern sizes in agitated fluids with a yield stress. *Chemical Engineering Communications*, *11*(1-3), 143–164.

Sossa-Echeverria, J., & Taghipour, F. (2014). Effect of mixer geometry and operating conditions on flow mixing of shear thinning fluids with yield stress. *AIChE Journal*, *60*(3), 1156–1167.

Sossa-Echeverria, J., & Taghipour, F. (2015). Computational simulation of mixing flow of shear thinning non-newtonian fluids with various impellers in a stirred tank. *Chemical Engineering and Processing: Process Intensification*, *93*, 66–78.

Stamhuis, E., & Thielicke, W. (2015). Pivlab-time-resolved digital particle image velocimetry tool for matlab.

Story, A., Story, G., & Jaworski, Z. (2021). Experimental and numerical investigation of axialand tangential forces in a stirred tank with yield-stress fluids. *Chemical and Process Engineering*, *42*(2).

Thompson, R. L., & Soares, E. J. (2016). Viscoplastic dimensionless numbers. *Journal of Non-Newtonian Fluid Mechanics*, *238*, 57–64.

Wheeler, A. J., Ganji, A. R., Krishnan, V. V., & Thurow, B. S. (2010). *Introduction to engineering experimentation* (Vol. 480). Pearson.

Zalc, J., Alvarez, M., Muzzio, F., & Arik, B. (2001). Extensive validation of computed laminar flow in a stirred tank with three rushton turbines. *AIChE Journal*, *47*(10), 2144–2154.